Impacts of Gravity Waves in the Martian Thermosphere: The Mars Global Ionosphere-Thermosphere Model Coupled with a Whole Atmosphere Gravity Wave Scheme

K. J. Roeten[1], S. W. Bougher[1], E. Yiğit[2], A. S. Medvedev[3], M. Benna[4,5], M. K. Elrod[4,6]

[1]Department of Climate and Space Sciences and Engineering, University of Michigan, Ann Arbor, Michigan, USA.

[2]Department of Physics and Astronomy, George Mason University, Fairfax, VA, USA.

[3]Max Planck Institute for Solar System Research, Göttingen, Germany

[4]Planetary Environments Laboratory, Code 699, NASA Goddard Space Flight Center, Greenbelt, Maryland, USA.

[5]CRESST II, University of Maryland, Baltimore County, Baltimore, Maryland, USA.

[6]CRESST II, University of Maryland College Park, College Park, Maryland, USA.

Key Points:

- Large-scale impacts of gravity waves in the thermosphere are examined using a modern gravity wave scheme in a Mars general circulation model
- Significant gravity wave momentum deposition is found in model simulations from 90-170 km altitude
- Gravity waves which propagate to the upper atmosphere of Mars can have an appreciable impact on thermospheric winds and temperatures

Corresponding author: K. J. Roeten, `kjroeten@umich.edu`

Abstract

Gravity waves are a key mechanism that facilitates coupling between the lower and upper atmosphere of Mars. In order to better understand the mean, large-scale impacts of gravity waves on the thermosphere, a modern whole atmosphere, nonlinear, non-orographic gravity wave parameterization scheme has been incorporated into a three-dimensional ground-to-exosphere Mars general circulation model, the Mars Global Ionosphere-Thermosphere Model (M-GITM). M-GITM simulations utilizing the gravity wave parameterization indicate that significant gravity wave momentum is deposited in the thermosphere, especially within the altitude range of 90-170 km. This impacts the winds in the thermosphere; in particular, M-GITM simulations show a decrease in speed of the wind maximum in the summer hemisphere by over a factor of two. Gravity wave effects also impact the temperatures above 120 km in the model, producing a cooler simulated thermosphere at most latitudes. M-GITM results were also compared to upper atmospheric temperature and wind datasets from the MAVEN (Mars Atmosphere and Volatile Evolution) spacecraft. Some aspects of wind data-model comparisons improved once the gravity wave scheme was added to M-GITM; furthermore, a cooler temperature profile produced by these new M-GITM simulations for the MAVEN Deep Dip 2 observational campaign resulted in a closer data-model comparison, particularly above 180 km. Overall, these modeling results show that gravity waves play an important role for the energy and momentum budget of the Martian thermosphere.

Plain Language Summary

Atmospheric gravity waves are an important physical process in the upper atmosphere of Mars. To better understand the average effects of gravity waves on the temperatures and winds above 100 km, a modern numerical scheme designed to represent the relevant physics has been added to a 3-D general circulation model, M-GITM (Mars Global Ionosphere-Thermosphere Model), which extends from the surface to about 250 km. Results from these M-GITM simulations show that in the upper atmosphere, the wind maximum in the summer hemisphere decreases in speed by over a factor of two once the effects of gravity waves are added to the model. Additionally, above 120 km, the model now produces a cooler upper atmosphere, on average. The new M-GITM results were also compared to select upper atmospheric temperature and wind datasets from the MAVEN (Mars Atmosphere and Volatile Evolution) spacecraft. Data-model comparisons in up-

–2–

per atmospheric wind speeds for a January 2017 observational campaign improve with the addition of gravity wave effects, as do data-model comparisons for upper atmospheric temperatures for a MAVEN Deep Dip campaign. Overall, these model results show that gravity waves can have significant impacts on the winds and temperature structure in the Martian upper atmosphere.

1 Introduction

Atmospheric gravity (or buoyancy) waves (GWs) are present in all stably strati-fied planetary atmospheres at all altitudes during all seasons with varying degree of in-tensity (Ando et al., 2015; Forbes et al., 2016; Yiğit & Medvedev, 2019). Due to their ability to transport energy and momentum upward, GWs are a key mechanism that drives vertical coupling between the lower and upper atmosphere (Yiğit & Medvedev, 2015). The divergence of the GW momentum flux due to wave dissipation and/or breaking pro-duces a body force that can accelerate or decelerate the mean flow at higher altitudes. Thus, understanding atmospheric coupling processes requires accurate quantification of the propagation and dissipation of gravity waves.

Recent missions to Mars have greatly improved our understanding of the planet's upper atmosphere; however, meaningful interpretations of the observed atmospheric vari-ability and explanations of the underlying physical mechanisms can be achieved to a greater degree if observations are supported by theoretical modeling efforts. Although many phys-ical and chemical processes responsible for the observed behavior of the upper atmosphere have been studied for decades (e.g., Bougher et al., 1990, 1993; Bougher et al., 2006), the impact of internal GWs on the Martian thermosphere has been explored to a lesser extent. This paper aims to provide comprehensive three-dimensional simulations of the winds and temperature of the Martian upper atmosphere, accounting for and quantify-ing subgrid-scale GW effects.

Development of Mars general circulation models (GCMs) extending from the ground to the exobase provides a unique opportunity to investigate vertical coupling processes that link the entire atmosphere (Bougher, Pawlowski, et al., 2015; González-Galindo et al., 2015). Through utilization of parameterization schemes, Mars GCMs can account for the missing effects of unresolved GWs from the troposphere to the thermosphere, sim-ilarly to what is done in GCMs of the terrestrial atmosphere (Yiğit et al., 2009). Recent

Mars GCM studies have used such schemes to study GW propagation into the thermosphere up to ~160 km (e.g., Medvedev et al., 2013, 2016; Yiğit et al., 2018). The first evidence that GWs which originate in the Martian troposphere can penetrate to the upper thermosphere was obtained in simulations with a linearized one-dimensional wave model (Parish et al., 2009). Later idealized numerical studies have supported this finding and further indicated that the associated GW drag is strong and sufficient for significant reduction, and even reversal, of the mean zonal jets in the mesosphere and lower thermosphere (MLT) region (100-130 km) (Medvedev, Yiğit, & Hartogh, 2011). This was demonstrated in the three-dimensional Mars GCM simulations of Medvedev, Yiğit, Hartogh, and Becker (2011), which interactively included a non-orographic, whole atmosphere, spectral gravity wave parameterization (Yiğit et al., 2008). In addition to the strong dynamical forcing from GW momentum deposition, further Mars GCM studies have shown that GWs significantly cool the lower thermosphere (Medvedev & Yiğit, 2012), facilitate CO_2 ice cloud formation (Yiğit et al., 2018), and modulate the circulation and temperature during global dust storms, thus changing the timing and intensity of the water transport into the upper atmosphere (Shaposhnikov et al., 2022).

While previous Mars GCM studies which included subgrid-scale GWs focused on altitudes below ~160 km, recent observations have provided further evidence that the upper atmosphere, even above these altitudes, is continuously populated by GWs of various spatiotemporal scales (e.g., Yiğit et al., 2021). GW-induced density perturbations in the Martian upper atmosphere have been identified from accelerometer-derived datasets from Mars Global Surveyor, Mars Odyssey, Mars Reconnaissance Orbiter, and ExoMars Trace Gas Orbiter (e.g. Fritts et al., 2006; Creasey et al., 2006; Tolson et al., 2007; Vals et al., 2019; Jesch et al., 2019). For example, Creasey et al. (2006) identified GWs with horizontal wavelengths of 100-300 km; these density perturbations associated with GWs also showed evidence of seasonal change. Additionally, GW momentum fluxes estimated from Fritts et al. (2006) were much larger than those seen at comparable densities at Earth, suggesting GWs would have considerable impact on large-scale mean velocities and their variability at Mars. The more recent MAVEN (Mars Atmosphere and Volatile Evolution) / NGIMS (Neutral Gas and Ion Mass Spectrometer) density dataset has also allowed for additional characterization of GW signatures throughout the thermosphere (e.g. Yiğit et al., 2015; England et al., 2017; Terada et al., 2017; Siddle et al., 2019). The perturbations of density associated with GWs have been observed at the lowest altitudes

–4–

of MAVEN's trajectory (∼125 km) (Siddle et al., 2019) and up to ∼250 km (Yiğit et al., 2015). Yiğit et al. (2015) found that in the upper thermosphere, density perturbations associated with GWs had amplitudes typically between 20-40% of the background density, with notable variability across local time, altitude, and latitude. At thermospheric altitudes, Terada et al. (2017) found that these wave structures have horizontal wavelengths between ∼100 and 500 km, while the amplitudes of these perturbations depend on the ambient temperature. England et al. (2017) similarly identified monthly-mean typical wavelengths of tens to hundreds of kilometers, in addition to determining that these GWs could generate heating/cooling rates of up to several hundreds of Kelvin per sol, in qualitative agreement with the predictions of Medvedev and Yiğit (2012) using a Martian GCM. A couple of different analyses of MAVEN/NGIMS densities showed that GW activity doubled during the 2018 Mars global dust storm (Leelavathi et al., 2020; Yiğit, Medvedev, et al., 2021).

Although analyses such as these suggest GWs are a regularly occurring phenomenon in the Martian upper atmosphere, the question of how to best represent GW effects in Mars GCMs is an active area of study and a still developing aspect of many Mars GCMs. Not all Mars GCMs currently include GW parameterizations, and many that do include them do not extend to the exobase. A recent review of GW effects in planetary atmospheres and approaches to their parameterization is given in the paper of Medvedev and Yiğit (2019).

The Mars Global Ionosphere-Thermosphere Model (M-GITM) is a ground to exobase 3-D Mars GCM that specializes in accurately representing the chemistry and physics relevant in the upper atmosphere. Previously, this model lacked a parameterization scheme for subgrid-scale GWs with non-zero phase speeds. While M-GITM has been able to reproduce many characteristics of the thermosphere reasonably well (e.g Bougher, Pawlowski, et al., 2015; Bougher, Roeten, et al., 2017), and agrees qualitatively with other models, there were notable differences in the zonal and meridional wind structure in the MLT region when compared to other Mars GCMs which utilize GW schemes. Furthermore, when M-GITM simulations were compared to MAVEN/NGIMS neutral thermospheric wind measurements, in certain cases, large differences were found between the observations and the model simulations, likely pointing to impacts on the thermospheric winds from some physical phenomenon lacking in the model (Roeten et al., 2019). Since GWs have significant thermal and dynamical impacts on the mean state of the upper atmo-

sphere (Yiğit & Medvedev, 2009; Medvedev et al., 2013), a GW parameterization scheme has been added into M-GITM to better understand the effects these subgrid-GWs have on the winds and temperature structure at thermospheric altitudes.

The rest of this paper is organized as follows: The numerical tools used - M-GITM and the GW parameterization scheme - are described in Section 2. Discussion of results from M-GITM simulations from two different seasons, solstice and equinox, are presented in Section 3. A series of sensitivity tests are discussed in Section 4, followed by two examples of comparisons between new M-GITM simulations and NGIMS datasets in Section 5. Conclusions and a summary of the findings can be found in Section 6.

2 Numerical Tools

2.1 The Mars Global Ionosphere-Thermosphere Model

M-GITM (Mars Global Ionosphere-Thermosphere Model) is a three-dimensional numerical model combining the original terrestrial GITM framework (Ridley et al., 2006) with Mars fundamental physical parameters, ion-neutral chemistry, and key radiative processes. While the primary aim of this model is to compute the basic observed features of the thermal, compositional, and dynamical structure of the Mars upper atmosphere, M-GITM is a whole atmosphere general circulation model and extends from the ground to ~250 km (Bougher, Pawlowski, et al., 2015). For the Mars lower atmosphere (below 100 km) physical parameterizations (e.g. solar heating, aerosol heating, CO_2 15-μm cooling) are taken from the NASA Ames Mars General Circulation Model (MGCM) code (Haberle et al., 1999). Empirical albedo and thermal inertia maps for the initial prescription of surface temperatures used in M-GITM are also the same as was employed in the NASA Ames GCM (Haberle et al., 1999). A basic Conrath scheme (Conrath, 1975) is employed for the dust vertical distribution, while using a globally-averaged and seasonally-averaged optical depth value (see Bougher, Pawlowski, et al. (2015)). For the Mars upper atmosphere (above ~100 km), physical processes and formulations for EUV-UV heating, dissociation, ionization, CO_2 15-μm cooling, and ion-neutral chemistry are taken from the Mars Thermosphere General Circulation Model (Bougher et al., 1999, 2000). Simulated M-GITM prognostic fields include neutral densities (e.g. CO_2, Ar, O_2, CO, N_2, O, N, He), ion densities (e.g. O_2^+, CO_2^+, O^+, N_2^+, NO^+), 3-component neutral winds (zonal, meridional and vertical), and neutral temperatures. Electron temperatures are empir-

–6–

ically prescribed from MAVEN observations (Ergun et al., 2015). Ion temperatures are based upon a Viking 1-2 empirical formulation from Rohrbaugh et al. (1979). M-GITM is run on a 5x5° regular horizontal latitude-longitude grid, with 2.5 km vertical resolution in altitude.

Recent updates to the M-GITM code, as seen in Roeten et al. (2019), include a fast non-local thermodynamic equilibrium (NLTE) CO_2 15-μm cooling scheme, adapted from González-Galindo et al. (2013). Its primary application is above $\sim$80 km where NLTE conditions prevail. Here, M-GITM simulated atomic O atoms collide with CO_2 molecules self-consistently, ultimately resulting in enhanced CO_2 cooling rates. Additionally, daily averaged solar EUV-UV fluxes are now incorporated in M-GITM from the Flare Irradiance Spectral Model - Mars (FISM-M) empirical model, a product generated from the MAVEN Extreme Ultraviolet Monitor (EUVM) measured solar fluxes (Thiemann et al., 2017; Eparvier , 2022). Finally, the EUV neutral heating efficiency in the thermosphere has been increased from 18% (the previous standard used in M-GITM) to 20% to better reflect recent findings from Gu et al. (2020).

A suite of M-GITM simulations have been compared with various MAVEN measurements obtained during its first three Mars years of operations. This includes measured densities and derived temperatures sampled during Deep Dip campaigns (e.g., Bougher, Jakosky, et al., 2015; Bougher, Pawlowski, et al., 2015; Zurek et al., 2017) as well as dayside science orbits (e.g., Bougher, Roeten, et al., 2017). Furthermore, a small set of MAVEN neutral thermospheric wind observations were compared with M-GITM velocities (Roeten et al., 2019). Simulations have also been conducted to compare to measurements obtained during the 2018 global dust storm (e.g., Elrod et al., 2020; Jain et al., 2020) and during solar flare events (e.g., Fang et al., 2019). Overall, MAVEN NGIMS, IUVS (Imaging Ultraviolet Spectrograph), and accelerometer measurements have been used extensively to validate the M-GITM code.

For the results shown in Sections 3 and 4 of this study, M-GITM simulations were run for 15 days, following a 20-day spin-up period to reach steady state conditions as the timeframe of interest is approached. These 15-day simulations have been averaged over all days and local times, retaining altitude and latitude information. Simulated fields have also been zonally averaged over all longitudes. Resulting zonally and temporally averaged fields will be described in this analysis. While several recent studies have iden-

214 tified substantial short time-scale variability (i.e. orbit-to-orbit variability) in thermo-

215 spheric density observations associated with GWs (e.g., Yiğit et al., 2015; England et

216 al., 2017), M-GITM is not designed to be able to replicate GW-induced variability on

217 such short time scales. Rather, the zonal and temporal averaging of M-GITM output

218 allows analysis of the large-scale impacts of GW effects on the temperature structure and

219 winds in the thermosphere.

2.2 The Whole Atmosphere Gravity Wave Scheme

221 Coarse-grid GCMs require appropriate GW parameterizations in order to account

222 for the effects of subgrid-scale waves. The whole atmosphere nonlinear GW parameter-

223 ization used in this study was initially developed for terrestrial GCMs and is fully de-

224 scribed in the work by Yiğit et al. (2008). Here we provide a concise characterization of

225 the scheme, its implementation into the M-GITM model, and its application in previ-

226 ous terrestrial and Martian studies.

227 The parameterization calculates a vertical evolution of GWs from their sources in

228 the lower atmosphere to the upper thermosphere. For this, first an appropriate distri-

229 bution of GW activity must be specified globally at a source level in the troposphere.

230 The wave activity is quantified in terms of the horizontal momentum fluxes $\overline{u'w'}$ as a func-

231 tion of horizontal phase speeds. An empirical Gaussian distribution of the momentum

232 fluxes is assumed. Then, the vertical evolution of the horizontal momentum flux of a har-

233 monic i with the phase speed c_i is given by

$$\overline{u'w'}_i(z) = \overline{u'w'}_i(z_0) \frac{\rho(z_0)}{\rho(z)} \tau_i(z) \tag{1}$$

234 where u' and w' are the horizontal and vertical components of the wind perturbations,

235 $\overline{u'w'}_i(z_0)$ is the momentum flux of the harmonic i at the launch (or source) level z_0, $\rho(z_0)$

236 is the background mass density at the source, and τ_i is the transmissivity of the given

237 wave, which controls the upward propagation of a given wave harmonic. If there are no

238 wave breaking and dissipation, harmonics propagate conservatively, and $\tau_i = 1$. Then,

239 the wave flux grows exponentially with height as the background density exponentially

240 decays with height. Otherwise, $\tau_i < 1$, which means that the exponential growth of the

241 wave flux is counteracted by wave breaking and/or dissipation. The transmissivity in-

242 cludes information on wave damping,

$$\tau_i(z) = \exp\left[-\int_{z_0}^{z} \beta_{tot}^i(z') \, dz' \right] \tag{2}$$

where the total vertical damping rate β_{tot}^i of a wave harmonic is a superposition of the damping due to molecular viscosity and nonlinear processes causing breaking/saturation (Medvedev & Klaassen, 2000):

$$\beta_{tot}^i = \beta_{mol}^i + \beta_{non}^i \tag{3}$$

Other dissipative processes such as wave damping due to ion friction β_{ion} and eddies β_{eddy} can be included, as is done for Earth (e.g., Yiğit et al., 2009; Medvedev et al., 2017). However, the former is small due to a lack of a strong global magnetic field on Mars and the latter is less constrained. Therefore, they have been excluded in this work. The β_{mol} and β_{non} terms are calculated using the same formulation as found in Yiğit et al. (2008) and Medvedev, Yiğit, Hartogh, and Becker (2011); see these for more detail.

Given a specified wave flux at the source level, z_0, Equation 1 can be integrated upward for each harmonic. The total momentum flux is the sum of all these components. The net acceleration or deceleration (i.e. GW drag) is given by the divergence of the flux divided by the mean density (Yiğit et al., 2008; Medvedev, Yiğit, Hartogh, & Becker, 2011), as seen in Equation 4 below. This GW drag is a source term that is added into the existing velocity equations in M-GITM.

$$a(z) = -\sum_i \frac{1}{\rho} \frac{\partial \rho \, \overline{u'w'}_i(z)}{\partial z} \tag{4}$$

The source of GW wave activity that needs to be specified in the lower atmosphere, from which upward computations are made by the GCM, is defined as a Gaussian spectrum in the form of:

$$\overline{u'w'}_i(z_0) = \text{sgn}(c_i - \overline{u}_0)\overline{u'w'}_{max} \exp\left[-\left(c_i - \overline{u}_0\right)^2/c_w^2\right] \tag{5}$$

This function which describes the GW spectrum has also been used in the application of this scheme in previous Mars modeling studies (Medvedev, Yiğit, Hartogh, & Becker, 2011; Medvedev & Yiğit, 2012; Medvedev et al., 2013), where its justification has been discussed. An example of the source spectrum for select values of the mean wind at the source level can be seen in Figure 1. In this calculation for the momentum flux at the source level, the spectra of phase speeds, c_i, are described by the maximum phase speed and the number of harmonics used. Here 30 harmonics are used, with horizontal phase speeds from -80 to 80 m/s. The half-width of the spectrum at half-maximum, c_w, was set at 35 m/s. The mean wind at source level, $\overline{u}_0$, is a value the parameterization scheme
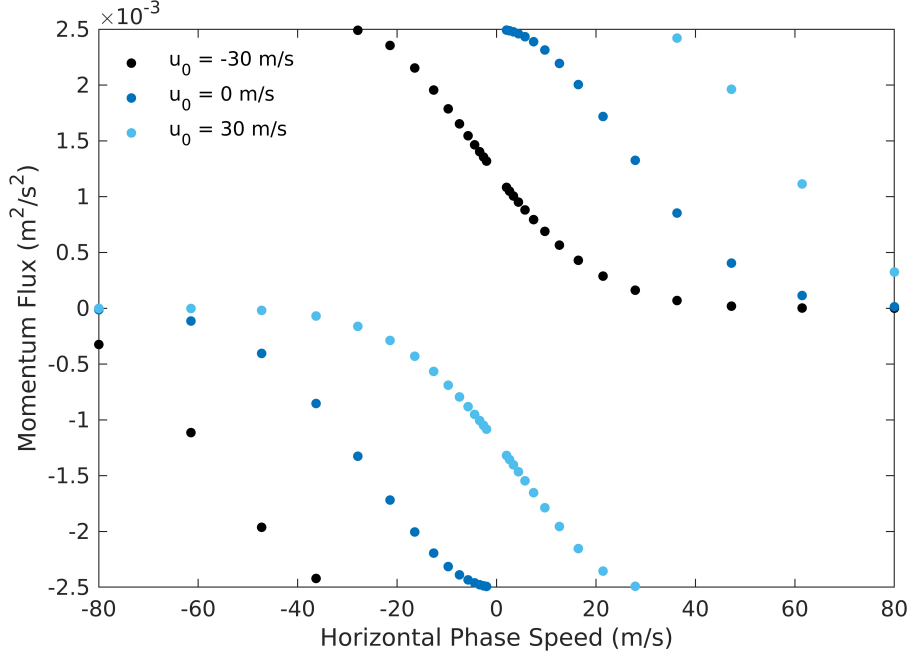
Figure 1. Examples of the type of GW momentum flux spectra at the source level used by the model. Different colors mark the fluxes for specific harmonics in three examples of potential source level winds, $u_0 = -30$, $u_0 = 0$, and $u_0 = 30$ m/s.

takes directly from M-GITM, but is typical of zero to tens of meters per second. The value of the maximum GW momentum flux at source level used is $\overline{u'w'}_{max}$=0.0025 m^2/s^2. This quantity has been commonly employed in previous Mars modeling studies using this GW scheme (e.g. Medvedev, Yiğit, Hartogh, & Becker, 2011; Medvedev & Yiğit, 2012; Medvedev et al., 2013, 2015; Shaposhnikov et al., 2019) and was recently estimated from occultation measurements with the ACS (Atmospheric Chemistry Suite) instrument onboard TGO (Trace Gas Orbiter) (Starichenko et al., 2021).

Somewhat better constrained is the horizontal wavelength of GWs in the Martian atmosphere, with estimates based on available observations ranging from tens of kilometers to hundreds of kilometers (e.g. Creasey et al., 2006; Fritts et al., 2006; Siddle et al., 2019) (see Section 1). In this GW scheme, a single representative wavelength for the most dominant subgrid-scale GWs is used, which facilitates computational efficiency, as is typically done in subgrid-scale GW studies. A horizontal wavelength of 300 km was utilized here, which is within the range of observationally estimated values.

Finally, the altitude of the source flux of GW momentum has been set at 8.75 km (roughly equivalent to the 260 Pa level employed by Medvedev, Yiğit, Hartogh, and Becker (2011) for this purpose). An altitude where weather processes are active, at or above the estimated average height of the convective boundary layer (Hinson et al., 2008) were the key considerations for the source level. This was done in order to reasonably represent the background winds near altitudes where non-orographic GWs may be launched. From this source level, the GW calculation is allowed to continue up to the top of the model, at 300 km.

In addition to the GW momentum deposition, the GW scheme also calculates the heating/cooling effects of GWs. In the scheme, the thermal effects of GWs are the sum of two terms, Q_{irr}^i, the heating due to irreversible conversion of mechanical wave energy to heat, and Q_{diff}^i, differential heating/cooling due to the divergence of the induced downward sensible heat flux (Medvedev & Yiğit, 2012). Similar to the GW drag, the GW thermal terms are summed over each wave harmonic and added to the existing energy equation in M-GITM. These thermal terms, as described in Medvedev and Yiğit (2012) are:

$$Q_{diff}^i = \frac{H}{2\rho R} \frac{\partial}{\partial z} \big[\rho a_i (c_i - \overline{u})\big] \tag{6}$$

$$Q_{irr}^i = \frac{a_i(c_i - \overline{u})}{c_p} \tag{7}$$

where H is the density scale height, ρ is the background mass density, R is the gas constant, a_i is the GW acceleration/deceleration, $\overline{u}$ is the local wind, and c_p is the specific heat at constant pressure.

In addition to the first use of this specific GW scheme in a Mars GCM (Medvedev, Yiğit, Hartogh, & Becker, 2011; Medvedev & Yiğit, 2012), it has been applied in an increasing number of Mars modeling studies, including on topics of Mars global dust storm effects on the upper atmosphere (Medvedev et al., 2013), as well as a comparison of thermal GW effects with CO_2 radiative cooling (Medvedev et al., 2015) and water transport to the upper atmosphere (Shaposhnikov et al., 2022). The most recent terrestrial application of the scheme has studied the influence of latitude-dependent GW sources on the vertical coupling between the lower and upper atmosphere, using the Coupled Middle Atmosphere Thermosphere-2 GCM (Yiğit, Alexander, & Ern, 2021). The scheme has been validated using other Earth GCMs as well (Miyoshi & Yiğit, 2019; Lilienthal et al.,

316 2020) and is a standard module of the Max Planck Institute Martian General Circula-

317 tion Model.

3 Impacts of Gravity Waves in M-GITM Simulations

319 MGCM simulations are presented in this section for solstice ($L_s = 270°$) and equinox

320 ($L_s = 180°$) conditions to study the impacts of GW effects in the upper atmosphere.

3.1 M-GITM Results from Solstice

322 The simulated zonal and meridional winds and the associated zonal and meridional

323 gravity wave drag are presented in Figure 2 for $L_s = 270°$, southern hemisphere sum-

324 mer solstice. Simulation results both with and without the GW scheme are shown in or-

325 der to demonstrate the effects of GWs on the circulation, especially in the thermosphere.

326 The region of the greatest GW momentum deposition (i.e., GW drag) calculated by the

327 whole atmosphere scheme occurs from ∼90-170 km, on average. During the southern hemi-

328 sphere summer solstice, the peak mean GW drag magnitude is found at high latitudes

329 in the southern hemisphere, where the absolute values reach 700 m/s/sol for the zonal

330 drag and 920 m/s/sol for the meridional drag. The mean zonal GW drag is primarily

331 directed eastward, except for a region at higher latitudes in the northern hemisphere,

332 ∼40-70°N. The mean meridional GW drag is primarily southward, except for some low-

333 magnitude northward drag at high latitudes in the northern hemisphere.

334 Notably, while the GWs dissipate over a broad range of altitudes in the upper at-

335 mosphere, the mean GW drag (for both the zonal and meridional components) calcu-

336 lated by M-GITM features a double maximum in altitude. The lower, narrower-in-altitude

337 drag maximum is centered around 100 km and has an extent of only about 10 km. The

338 other drag maximum occurs over a broader range of altitudes, from about 120-160 km.

339 GWs break and/or saturate at different locations in the whole atmosphere system de-

340 pending on wave characteristics such as phase speed as well as on the characteristics of

341 the background atmosphere. It is likely that the lower altitude population seen in Fig-

342 ure 2 is produced by nonlinear breaking/saturation, while the one at higher altitudes is

343 due to exponentially increasing molecular diffusion and thermal conduction.

344 While there is a limited number of other modeling studies that both include a non-

345 orographic GW scheme and extend through the thermosphere, these M-GITM calcula-

tions of GW drag in the thermosphere can, in part, be compared to those from Medvedev, Yiğit, Hartogh, and Becker (2011), whose MGCM extended up to ∼130 km. The magnitude of temporally and zonally averaged GW drag of hundreds of meters per second per sol, up to 700 m/s/sol for the zonal GW drag, found by Medvedev, Yiğit, Hartogh, and Becker (2011) within the altitude range of approximately 100-130 km from their $L_s = 270°$ solstice simulation is comparable to that calculated by M-GITM. For zonal GW drag, while model simulations from both of these studies produce eastward drag in the southern summer hemisphere and westward drag in the northern winter hemisphere at middle-high latitudes within this altitude range, M-GITM produces larger GW drag in the southern hemisphere while the Medvedev, Yiğit, Hartogh, and Becker (2011) study produces greater magnitudes in the northern hemisphere. This could be related to the slower eastward winds in the northern hemisphere produced by M-GITM than those that are seen in the solstice simulations from Medvedev, Yiğit, Hartogh, and Becker (2011).

Figure 2 also shows that the GW drag calculated by M-GITM in the thermosphere primarily acts against the predominant zonal wind, resulting in a slower mean flow. This is most noticeable starting at approximately the same altitude range over which the GW drag magnitude is the greatest. For the zonal wind (in the top row of Figure 2) it can be seen that without including the effects of GWs, the model produces high-speed winds throughout the upper portion of the model domain, which are on average westward. Once the GW scheme is included, this splits into a notably slower upper thermospheric wind maximum and a middle atmospheric jet around 50 km, with the region between (∼100-150 km) now having average velocities of 20-40 m/s. From ∼100 km to the top of the model, with the addition of the GW scheme, mean westward speeds have decreased by up to ∼150 m/s and a better defined eastward flow appears in the northern hemisphere. This weakening of the zonal wind speed and closing off of the upper extent of the middle atmospheric jet is a characteristic feature of the mesosphere and the lower thermosphere region on Earth and Mars due to GW momentum deposition and has also been seen in other studies (e.g., Medvedev, Yiğit, Hartogh, & Becker, 2011; Kuroda et al., 2016; Watanabe & Miyahara, 2009; Miyoshi & Yiğit, 2019; Yiğit, Alexander, & Ern, 2021).

For the meridional winds, the GW drag also primarily acts against the mean flow in the upper atmosphere. This results in near-zero average velocities near the same altitude range where the maximum GW drag is deposited, or even reversals in the average flow direction at middle-to-high latitudes in both hemispheres. The decrease in ve-

–13–

locity between the M-GITM simulations without and with GW effects can reach ∼40 m/s. This difference is not as large as was seen for the mean zonal winds, which might be expected since the mean meridional wind speeds in the initial no-GW simulation are much weaker than the zonal speeds. In addition to the large decrease in wind speed in the MLT region, the mean flow at most latitudes in the thermosphere is found to decrease in magnitude once the GW scheme is added, similar to the mean zonal wind.

The impacts of adding the GW scheme to M-GITM also appear in the zonally averaged temperature structure presented in Figure 3. The mean temperatures simulated in the thermosphere above ∼120 km are significantly cooler with the effects of GWs included, by up to 50 K. The greatest difference is seen at high latitudes in the northern winter hemisphere and at middle to high latitudes in the southern summer hemisphere. This is similar to what was found in Medvedev and Yiğit (2012), wherein after adding a GW parameterization scheme to a MGCM, resulted in temperatures at middle-to-high latitudes in the thermosphere (up to ∼150 km, the top of the model) cooling by up to 45 K compared to their simulation without GW effects. In addition to the changes in the thermosphere, as seen in Figure 2 in the middle atmosphere in the southern summer hemisphere, from about 50-100 km, the GW scheme produces somewhat warmer averaged temperatures in M-GITM than in the case without GW effects, by up to 20 K at the higher latitudes. This difference, however, is not as large in magnitude as is the temperature difference produced in the thermosphere.

The changes in temperature in the middle and upper atmosphere can have contributions both from changes in the large-scale dynamics that result in modified advection and adiabatic heating/cooling, as well as irreversible wave heating and heating/cooling due to divergence of wave flux, the latter two of which are accounted for within the GW scheme. These latter two, when combined, show the net GW heating or cooling calculated directly by the GW scheme. For the solstice, the mean rate of net GW heating in the thermosphere approaches ∼400 K/sol at high latitudes, particularly in the southern hemisphere. This is somewhat greater than the ∼200 K/sol from the solstice simulations of Medvedev and Yiğit (2012), though within the same order of magnitude.

–14–
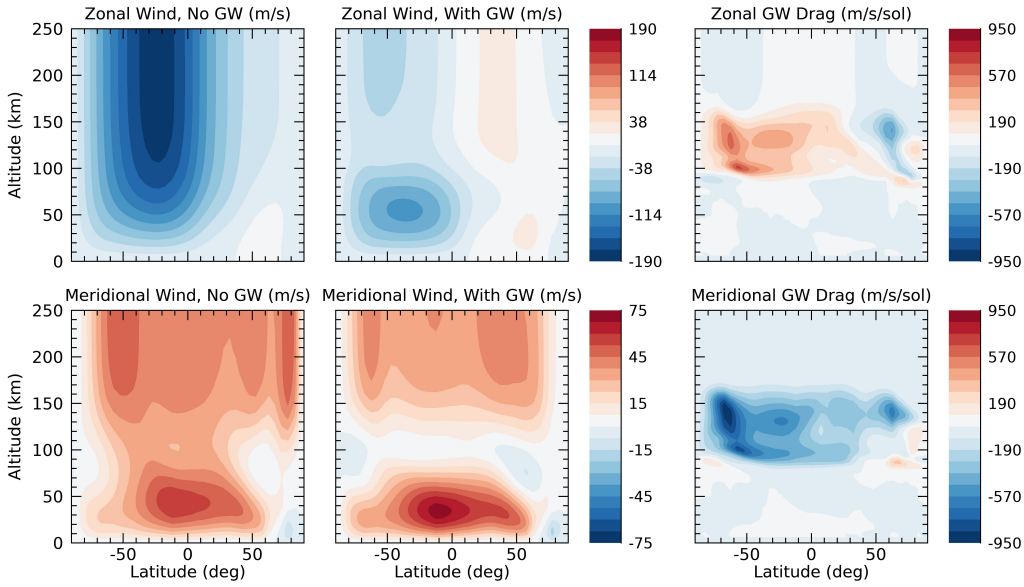
Figure 2. Zonally averaged zonal (top row) and meridional (bottom row) wind and GW drag from M-GITM, each also averaged over 15 days starting at $L_s = 270°$ (southern hemisphere summer solstice). The left column of plots shows the simulated wind velocity components when the effects of GWs are not included in M-GITM, while the middle column is the same but for when the effects of GW are included. The right column shows the averaged zonal and meridional GW drag.
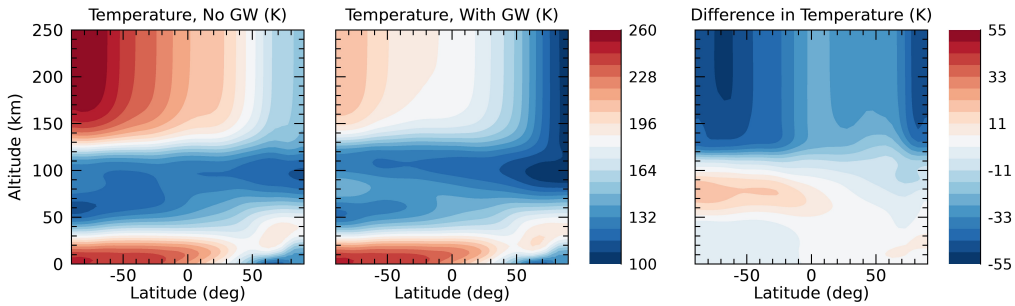
Figure 3. Zonally averaged temperature, also averaged over 15 days starting at $L_s = 270°$. The left column of plots shows the simulated temperatures when the effects of GWs are not included in M-GITM, while the middle column is the same but for when the effects of GWs are included. The right column shows the difference between the two (GW case - no GW case).

3.2 M-GITM Results from Equinox

During the $L_s = 180°$ equinox (southern hemisphere vernal equinox), after adding the GW scheme to M-GITM, a similar response can be seen in the upper atmosphere as occurred in the solstice simulation, though slightly subdued in comparison due to the slower mean winds this time of year. The general effect of the different season can also be observed in a more symmetrical distribution of wind velocities and corresponding GW drag with latitude in the equinox case.

The averaged GW drag calculated by M-GITM for the $L_s = 180°$ equinox can be seen in the two panels in the right column of Figure 4. For the zonal GW drag, the greatest mean magnitudes are in a narrow band from ∼90-110 km, with the largest values of nearly 900 m/s/sol found at high latitudes. Regions of significant GW drag at higher altitudes, from ∼120-180 km, can also be seen, especially at higher latitudes. At these altitudes, eastward zonal drag extends throughout the low and middle latitudes; at higher latitudes, the averaged zonal GW drag is westward. The greatest mean meridional GW drag (up to 735 m/s/sol) is seen at high latitudes. Again, a double maximum feature in altitude can be seen, with a narrow band of GW drag around 90-110 km, and a broader drag maximum from ∼120-160 km. Like the mean zonal GW drag at high latitudes, the two maxima of mean meridional drag at these two different altitude ranges switch sign, though unlike the high latitude zonal GW drag, different hemispheres exhibit opposing senses of that sign.

Comparing the magnitude of zonal GW drag calculated by M-GITM between ∼100-130 km to that found in simulations from Medvedev, Yiğit, Hartogh, and Becker (2011) for the $L_s = 180°$ equinox, it can be seen that while both simulations have mean GW drag with orders of magnitude of hundreds of meters per second per sol, M-GITM values can be larger by a factor of two. Also, while Medvedev, Yiğit, Hartogh, and Becker (2011) find meridional GW drag to be about three times weaker than the zonal GW drag in their MGCM, the difference between M-GITM zonal and meridional GW drag magnitudes is much less notable.

The left two columns of Figure 4 show the average zonal and meridional winds from the M-GITM equinox simulations, without and with subgrid GW effects included. When the GW scheme is added to M-GITM, the average zonal wind magnitude has a maximum of 40 m/s, with the largest averaged speeds found in the middle atmosphere rather

–16–

than the thermosphere. Like for the solstice, the overall effect of GWs is to produce much slower mean winds throughout the thermosphere compared to the case when GW effects are not included, decreasing by as much as 100 m/s at these altitudes. The greatest impact is seen at middle-to-high latitudes above 100 km, where the inclusion of the GW drag results in a reversal of the flow from westward to light eastward winds, on average.

The addition of the GW scheme produces more complex changes in the mean meridional velocities. Most notably, starting around 120 km, the mean meridional velocities undergo a reversal in direction with the addition of subgrid-scale GWs. Above the altitude level that this reversal initially takes place, mean meridional speeds have increased in magnitude in the upper thermosphere slightly, but now have the opposite direction to that found in the case without the GW scheme.

Similar to the solstice simulation, adding the GW scheme to M-GITM in the equinox simulation again results in a much cooler thermosphere (above ∼90 km) on average compared to the run without GW effects, as seen in Figure 5. While the thermosphere appears cooler at all latitudes, the greatest difference (by up to ∼50 K, on average) between these two cases is found at high latitudes. Unlike in the solstice case, the addition of the GW scheme does not result in notably warmer temperatures in the middle atmosphere, instead remaining close to the same values between both simulations.

4 Sensitivity Tests

All atmospheric parameterizations include certain empirical (or tunable) parameters that act to quantify different aspects of the unresolved phenomena. In order to ascertain the sensitivity of M-GITM to the tunable parameters within the GW scheme, a series of tests were done. These tests were conducted with the characteristic horizontal wavelength, source flux magnitude, the maximum phase speed, spectrum half-width, number of harmonics, source height, and maximum height of allowed wave propagation. Here, the results from a subset of the simulations from the northern winter solstice ($L_s = 270°$) are described, namely, sensitivity tests with the horizontal wavelength and the maximum source flux. Adjustments to these two parameters produced some of the most significant changes in the model output compared to the other tunable parameters. All of these tests were performed with the same M-GITM set-up as described in Section 2.1, with the only differences being the change in the value of the selected parameter. Sim-

–17–
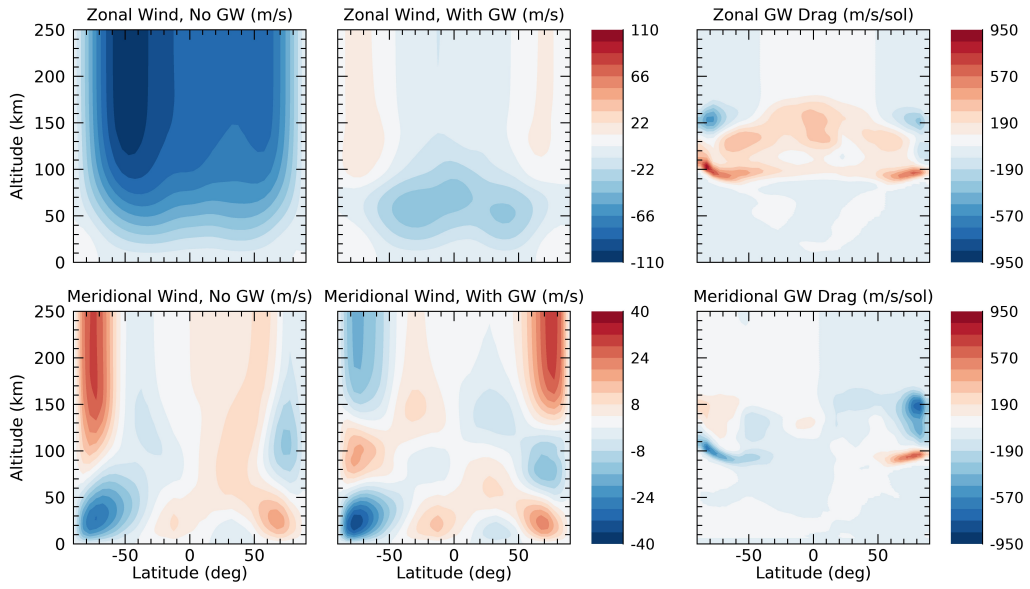
Figure 4. Same as Figure 2, but for the $L_s = 180°$ equinox (southern hemisphere vernal equinox).
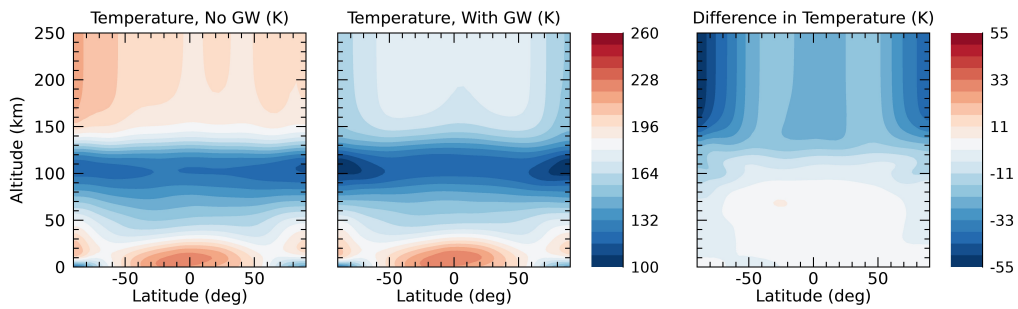


Figure 5. Same as Figure 3, but for the $L_s = 180°$ equinox.

ilar to the results shown in previous sections, the M-GITM results shown here are 15-day mean, zonally averaged fields. Plots of M-GITM results with these variations in maximum source flux and horizontal wavelength are included in Figures 6 and 7, respectively.

As described in Section 2.2, the source flux included in the GW scheme is based on a Gaussian distribution, which is allowed to be shifted by the background winds at the source level z_0, with the maximum source flux $\overline{u'w'}_{max}$ value as a tunable parameter based on previous estimates of GW source strength on Mars (Medvedev, Yiğit, & Hartogh, 2011). For the sensitivity tests, the baseline value of the maximum source flux, 0.0025 m^2/s^2, has been decreased to 10% of the baseline value (0.00025 m^2/s^2) and increased by a factor of two from the baseline (0.005 m^2/s^2). While this parameter is currently poorly constrained due to a scarcity of available observations, this range is one that has also been employed by other Mars GCMs that have implemented this GW scheme (e.g., Medvedev et al., 2013, 2015; Yiğit et al., 2018).

The horizontal wavelength of gravity waves is somewhat better constrained by available observations at Mars, particularly with new MAVEN data. At thermospheric altitudes, analyses of perturbations in NGIMS density observations (assuming along-track variation is horizontal), was found to be 200-400 km by Terada et al. (2017) and 100-300 km by Siddle et al. (2019). A similar range for horizontal wavelength was identified by Creasey et al. (2006) of 100-300 km from Mars Global Surveyor accelerometer data. For our sensitivity tests with M-GITM, the horizontal wavelength was decreased from 300 to 200 km, a value within the ranges previously suggested by data analysis.

In these M-GITM simulations, the effects of changing the maximum source flux shifts the altitudes of the most significant GW momentum deposition (see Figure 6). For the case in which the maximum source flux is increased by a factor of two, the lower edge of the region of maximum GW drag (both zonal and meridional) is found at $\sim$90 km in the summer hemisphere ($\sim$80 km in the winter hemisphere) while for the case with maximum source flux at 10% of baseline value, the lower edge of this region has shifted to $\sim$110 km in the summer hemisphere ($\sim$100 km in the winter hemisphere). In the 10% of baseline value case, the altitude of the lower maxima shifted to high enough altitudes that the two distinct altitude bands with GW drag maxima have seemingly merged into one. This produces a greater maximum GW drag magnitude than in either the baseline case or the case with the factor of two increase in maximum source flux. Hence, with a

–19–
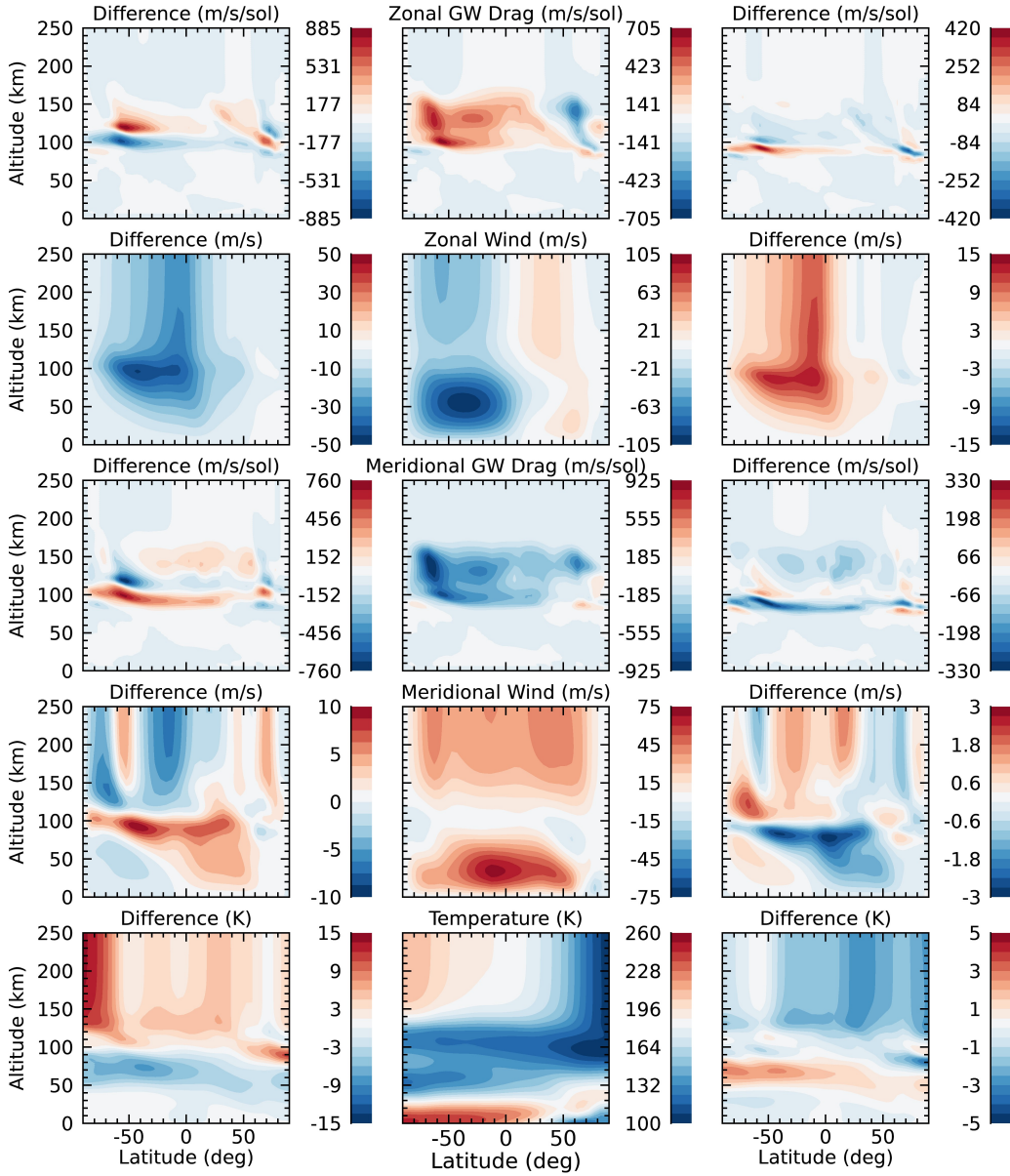
Figure 6. M-GITM results showing model response to adjusting the maximum flux of the source GW spectrum. The left column shows the differences between the baseline case and the case with the maximum source flux at 10% of the baseline value (0.00025 m^2/s^2), the middle column shows the baseline case (0.0025 m^2/s^2), and the right column shows the differences between the baseline case and the factor of two increase from the baseline value (0.005 m^2/s^2). Rows show, from top to bottom, zonal GW drag, zonal wind, meridional GW drag, meridional wind, and temperature. All plots show 15-day time averaged and zonal mean fields.
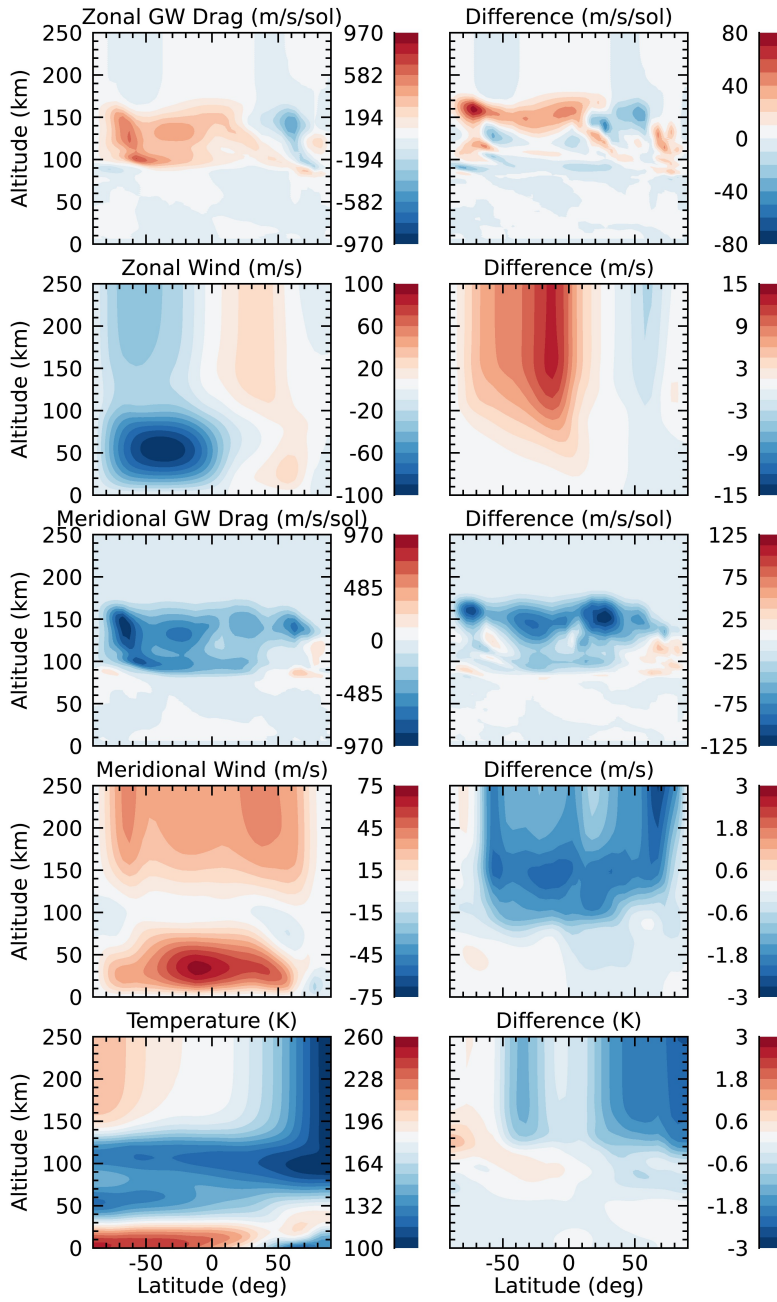
Figure 7. M-GITM results showing model response to adjusting the horizontal wavelength used in the GW scheme. The left column shows the case where the horizontal wavelength has been decreased to 200 km and the right column shows the differences between the baseline value (300 km) and the case with a horizontal wavelength of 200 km. Rows show, from top to bottom, zonal GW drag, zonal wind, meridional GW drag, meridional wind, and temperature. All plots show 15-day time averaged and zonal mean fields.

greater maximum source flux, significant wave breaking and/or saturation occurs at slightly lower altitudes. To a lesser degree, the edge of the GW drag maxima at higher altitudes also shifts upward in altitude as the maximum source flux increases, but only by ∼5 km or less in these cases. Overall, the combination of these effects demonstrates that as maximum source flux increases, waves of different phase speeds break and/or saturate across a slightly wider range of altitudes in the upper atmosphere.

Figure 6 also indicates that as the maximum source flux increases, mean westward wind velocities in the summer hemisphere decrease in magnitude. A greater change in the mean zonal wind velocities is found between from the 10% of baseline value case and the baseline case than from the baseline case to the case with the factor of two increase in maximum source flux. These differences are on the order of several tens of meters per second and 10 m s^{-1}, respectively. Mean meridional velocities show differences from the baseline case up to 10 m/s. In the thermosphere as the maximum source flux increases, the mean northward meridional speed decreases in the higher latitudes while increasing at low latitudes.

The zonal mean temperatures become cooler at most latitudes above ∼120 km as the source flux increases, except for a region of the northern hemisphere middle latitudes ($\sim 55-65°$) in the case in which the maximum source flux increases by a factor of two, which warms by several degrees. From the case with 10% of the baseline source flux to the baseline case, the greatest averaged temperature difference is nearly 15 K lower in the southern hemisphere at high latitudes and above 120 km. There is also a region of warming from 40-90 km, particularly in the summer hemisphere. Examining the differences between the baseline and two times increase in source flux shows a slightly different pattern above 120 km. While most of the thermosphere cools in comparison to the baseline case (except for southern mid-latitudes), the greatest change is lower temperatures in the northern middle to high latitudes, though with only a few degrees Kelvin of difference.

Results from the sensitivity test in which horizontal wavelength was decreased from the baseline value of 300 km down to 200 km are shown in Figure 7. For the zonal and meridional GW drag, the changes occur primarily in the upper altitude part of the area of maximum drag (∼140-170 km), while the lower extent of this region (∼90-140 km) experiences relatively little change from the baseline case. On average, an increase in mag-

–22–

nitude on the order of several tens of meters per second per sol for zonal GW drag and up to 100 m/s/sol for meridional GW drag is found in the higher altitude region and across most latitudes, except for higher latitudes in the northern winter hemisphere. Unlike the source flux sensitivity tests, essentially no shifting of the altitude range of the region of most significant GW drag occurs.

Additionally, in these M-GITM simulations, as the horizontal wavelength decreases, the magnitude of the westward mean zonal wind speeds in the thermosphere decreases by up to $\sim$10 m/s on average. Unlike the tests with varying source flux, which results in notable changes in the middle and upper atmosphere in the summer hemisphere, these simulations primarily show changes in the mean zonal winds above $\sim$90 km in the summer hemisphere. The differences in meridional winds are smaller on average, with changes on the order of a few meters per second above $\sim$90 km. The changes in the meridional wind velocities consist predominantly of a decrease in the northward winds across all latitudes.

The zonally averaged temperatures respond slightly differently to the changed horizontal wavelength than they do to changing the maximum source flux as well. Averaged difference in temperature is on the order of a few degrees Kelvin throughout the domain. Similar to increasing the source flux, decreasing the horizontal wavelength also results generally in a cooler thermosphere, with greatest changes seen at high latitudes in the northern winter hemisphere. However, in the southern summer hemisphere, slightly warmer averaged temperatures are found at latitudes above $\sim 50^\circ$ above 100 km as well as at latitudes down to $\sim 0^\circ$ at altitudes of $\sim$80-120 km.

Overall, the relatively small differences in M-GITM simulations using either 200 km or 300 km for the horizontal wavelength indicate that the scheme is robust with respect to the expected values for this parameter. Somewhat larger changes are observed when the source flux magnitude is changed, particularly when it was adjusted by an order of magnitude. However, the changes in the simulated fields generated when the scheme itself is added to M-GITM are still larger in magnitude than in these sensitivity tests (i.e. Figures 2 and 3). If evidence were found in future data analysis that suggested the source flux was significantly different under certain atmospheric conditions than what was used here, under these new constraints, the altitude range where the most significant GW drag is deposited could shift further. As demonstrated in these tests, this would impact both

–23–

the simulated mean wind speeds in the upper atmosphere as well as the temperature struc-

ture.

5 Data-Model Comparisons with MAVEN/NGIMS and M-GITM

In order to further study the impacts of the GW scheme in M-GITM, as well as to examine how well these new M-GITM simulations replicate observed thermospheric conditions, select data-model comparisons have been conducted. Two in-situ datasets (Benna et al., 2015) from the NGIMS instrument onboard the MAVEN spacecraft were used in comparison with simulated thermospheric fields from M-GITM. NGIMS is a quadrupole mass spectrometer designed to characterize the neutral and ion composition of the upper atmosphere of Mars. It has a vertical resolution of 5 km and target accuracy of <25% for most species, with observations generally taken from ∼150 km altitude through the exobase (Mahaffy, Benna, King, et al., 2015; Mahaffy, Benna, Elrod, et al., 2015).

5.1 M-GITM Comparisons with NGIMS Derived DD2 Temperatures

The first dataset used is the Level 2, Version 8, Revision 1 (V08R01) data product which consists of fully calibrated single species abundances (Mahaffy, Benna, Elrod, et al., 2015). These NGIMS densities were then converted into temperatures using the method described in Bougher, Roeten, et al. (2017). A similar method is also used in Stone et al. (2018) and Snowden et al. (2013) to calculate temperature profiles. In this method, the hydrostatic equation is vertically integrated (assuming the vertical density profile is in hydrostatic equilibrium) using NGIMS Argon density profiles to find the local partial pressure. Profiles tend to converge below a certain altitude range regardless of the of upper boundary conditions used, as long as it is within a realistic range. This altitude range was identified to be generally between 200-220 km for perihelion conditions and 190-200 km for aphelion conditions (Bougher, Roeten, et al., 2017). As such, temperature profiles for this study are only analyzed below these altitude ranges for the appropriate season. Furthermore, since the spacecraft's trajectory has a larger horizontal component near periapsis, and the hydrostatic method for deriving temperatures assumes a vertical integration, roughly a scale height at the bottom of the profile has been left out of the analysis. Finally, temperature profiles are calculated from the local partial pressure and Ar densities using the ideal gas law. Ar densities are used since the gas is immune to buffering by interactions with the instrument walls, unlike other reactive

–24–

species (Mahaffy, Benna, Elrod, et al., 2015). In order to remain consistent with previous studies that have derived temperature profiles from NGIMS data (e.g., Bougher, Roeten, et al., 2017; Stone et al., 2018), only the inbound segment of Ar observations are used in this analysis.

Early in the MAVEN mission, the spacecraft completed several week-long campaigns to lower the nominal science orbit periapsis altitude from ∼150 km down to ∼125 km (Jakosky et al., 2015). One of those campaigns, called Deep Dip 2 (DD2) is used in this analysis to compare to the updated M-GITM simulations. DD2 spans MAVEN orbits 1059-1086, over the southern low-latitudes (22°S to 11°S) during the late southern hemisphere summer ($L_s \sim 330°$), near noon (11-12 LT). Density profiles from these orbits have been averaged to produce a single campaign-averaged profile. This averaging is done over longitude and time (i.e. orbit), preserving latitude and altitude information along the track. Latitude and local time only precess slightly between sampling points at similar altitudes in consecutive orbits.

M-GITM simulations to compare to the DD2 campaign were run for the same time period the campaign took place, utilizing the appropriate FISM-M solar fluxes (Thiemann et al., 2017; Eparvier , 2022) derived from EUVM observations during the campaign. Note that the values of the GW parameters used within the DD2 M-GITM simulations are the same as those used in the $L_s = 270°$ baseline GW case described in Section 3.1. From these simulations, for each orbit in DD2, temperature and density profiles were extracted along the same trajectory flown by MAVEN in latitude, local time, and altitude. These M-GITM 'flythroughs' correspond to each MAVEN orbit during the campaign. A conversion between the aerocentric coordinate system native to the model and the aerodetic coordinate system used by NGIMS was also implemented in this process. The resulting M-GITM flythroughs allow for a more direct comparison between output from the model and in-situ NGIMS data. Inbound segments of M-GITM DD2 flythroughs were then averaged together in the same manner as was done for the calculated NGIMS density profiles to produce a campaign averaged profile.
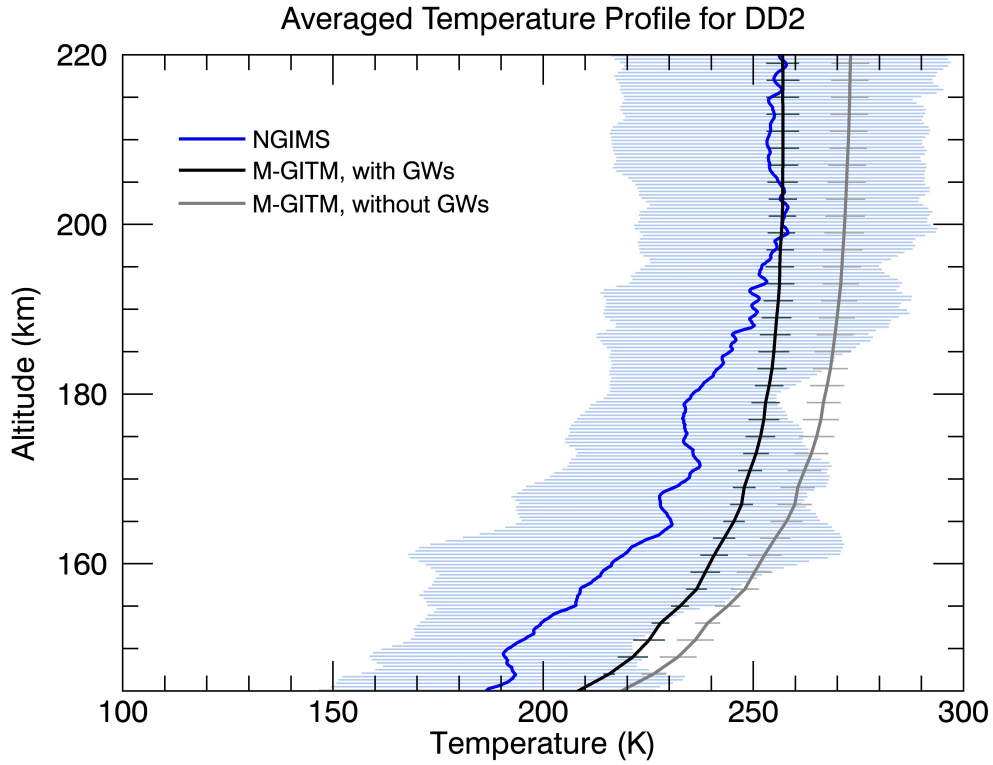
Figure 8 shows the averaged NGIMS temperature profile from DD2 and two averaged M-GITM profiles, one which takes into account the effects of subgrid GWs, and one which does not. The original M-GITM profile, which does not utilize the GW parameterization scheme, is nearly 20 K warmer than the NGIMS DD2 profile at the top

–25–

of this altitude range (near the exobase) and up to nearly 30 K warmer at 180 km and below. Once the GW scheme is added to the model, the temperature profile becomes ∼15 K cooler near 220 km to ∼10 K cooler by 150 km. This results in M-GITM reproducing the observed temperatures from 200-220 km. Though the differences between simulated and observed temperatures are greater below these altitudes, adding the GW scheme does still notably improve the comparison. At the altitudes of ∼140-190 km for DD2, the mismatch between data and model may be due to low atomic O abundances simulated in the model with respect to NGIMS measured values (Bougher, Brain, et al., 2017). Future work will require a sensitivity analysis to address the impact of variable eddy coefficients upon atomic O and the resulting dayside temperatures in M-GITM for DD2 conditions.

5.2 M-GITM Comparisons with NGIMS Wind Campaigns

In addition to the nominal density dataset, NGIMS has been able to provide in-situ measurements of neutral thermospheric wind velocities. These wind observations provide a way to more directly test the dynamics and circulation produced by M-GITM, though on a somewhat limited case-by-case basis. Two of these wind measurement campaigns were utilized in this analysis for data-model comparison.

The NGIMS neutral wind dataset has been generated through a novel observational technique whereby the boresight of the NGIMS instrument onboard MAVEN is rapidly and continuously varied though the instrument platform nodding ±8° off the ram direction. Wind velocities are then determined from the observed modulations of neutral and ion fluxes as the instrument pointing direction is changed. A detailed explanation of how NGIMS carries out this measurement can be found in the work by Benna et al. (2019). The thermospheric wind is sampled every ∼30 s along an altitude range of ∼140 up to 220 km. Along- and across-track wind magnitudes have an uncertainty typical of 20 and 6 m/s, respectively. Uncertainties are dominantly due to errors in the reconstructed spacecraft ephemeris and the instrument boresight direction, the energy resolution of NGIMS's mass filter, and in counting statistics (Benna et al., 2019). In order for the horizontal winds to be determined, it is assumed that vertical winds are negligible and that horizontal winds do not change on time scales shorter than the 30 s it takes for the instrument boresight direction to complete a full motion cycle. Since nominally, the Martian atmosphere is in hydrostatic equilibrium, vertical velocities might be expected to remain

Figure 8. Averaged NGIMS and M-GITM temperature profiles for the NGIMS Deep Dip 2 (DD2) campaign. The blue profile shows the temperature profile derived from NGIMS Argon densities. The black and gray profiles are extracted from M-GITM simulations for the same DD2 time period and trajectory flown by MAVEN/NGIMS, with the black profile showing results for the case with the effects of subgrid GWs included, and the gray profile showing results for the case without the effects of subgrid GWs. The horizontal bars along the profiles indicate one standard deviation of orbit-to-orbit variability.

Table 1. Characteristics of NGIMS Wind Campaigns used in Data-Model Comparisons

Date	Orbits	Local Time (hr)	Latitude (deg)	L_s (deg)[a]
11–13 January 2017	4437–4446	23–1	38°S–66°S	297
30 May – 1 June 2017	5170–5179	10–11	30°N–61°N	12

[a]Approximate solar longitude

small if not driven by extreme solar events like flares (Bougher, Pawlowski, et al., 2015). In addition, Benna et al. (2019) found good fits between observations over the 30 s sampling period to the expected modulation in fluxes if constant winds over this time was assumed, indicting no appreciable uncertainty is added due to <30 s wind variations. Zonal and meridional neutral wind measurements from the NGIMS Level 3, Version 3, Release 1 (V03R01) dataset were used in this study.

NGIMS wind measurements are generally conducted in campaigns occurring monthly, each with 5-10 consecutive orbits of wind observations taken along MAVEN's track through the thermosphere (passing through the same latitudes, local times, and altitudes, but different longitudes throughout a single campaign). Two examples of these wind observational campaigns, the January 2017 and May 2017 campaigns, are presented with corresponding M-GITM simulations. Specific characteristics of these campaigns can be found in Table 1. For each campaign, measurements in each orbit are averaged together over time and longitude to produce a single profile along MAVEN's trajectory in latitude, local time, and altitude, in a similar manner done with the NGIMS campaign-averaged temperature and density profiles in the previous section.

The M-GITM simulations run for both these wind campaigns utilize the same GW parameters as used in the $L_s = 270°$ baseline case from Section 3.1, with the only differences being the dates, orbital parameters, and solar flux. Model wind flythroughs were done in the same manner as was done for temperature flythroughs for DD2, extracting M-GITM output along the same latitude, local time, and altitude track traversed by MAVEN each orbit during the campaign. These were then likewise averaged (keeping the inbound and the outbound segments of each orbit separate) to produce a campaign-averaged profile that tracks over latitude, local time, and altitude.

–28–

The January 2017 campaign took place near perihelion, at midnight local time, and southern middle-to-low latitudes (see Table 1) and is shown in Figure 9. Prior to adding the GW parameterization scheme to M-GITM, the simulated speed along the averaged profile was in the range of 200-300 m/s faster than the averaged speeds observed by NGIMS, with an equally poor match in averaged direction along the profile. This has also been noted in an earlier data-model analysis of this campaign from Roeten et al. (2019). By accounting for subgrid-scale GWs, the average speed profile slows by over 100 m/s, reducing differences between the observed and modeled speeds to less than 100 m/s on the outbound segment of the NGIMS trajectory and from 0-50 m/s on the inbound segment. This is a significantly improved match to the NGIMS campaign-averaged speed when compared to the thermospheric wind speed predicted by M-GITM when subgrid GWs were not accounted for, and suggests that GW effects are a significant factor in producing the observed mean flow speeds in this latitude-LT sector for this campaign.

Additionally, with the inclusion of the GW scheme, the simulated averaged wind direction for this campaign also shifts, now having less strong of a westward component while retaining the northward component. However, this change does not notably reduce differences in direction between mean observations and model flythroughs. This might, in part, be due to the significant orbit-to-orbit and sampling-point-to-sampling-point variability observed during this campaign, reported by Roeten et al. (2019). The high amount of variability makes the interpretation of the average direction difficult. Furthermore, this level of small-scale variability, whether it be temporal or spatial variability (or both) cannot be replicated by M-GITM. Though observations suggest GWs produce significant variability in the thermosphere (e.g., Yiğit et al., 2015), M-GITM cannot produce these individual perturbations; rather, the GW scheme introduced in M-GITM was designed to account for quantities averaged over the wave phases, in particular the momentum flux. While the significant directional variability in this case will make the average direction difficult for M-GITM to reproduce regardless of the addition of the GW parameterization scheme, the notable improvement in the mean speed for this campaign once the GW scheme is added suggests that M-GITM is better capturing a key atmospheric process.

The May 2017 campaign occurred near northern hemisphere vernal equinox, on the dayside, and at northern middle latitudes (see Table 1). In the M-GITM run without the GW scheme, as shown in Figure 10, the outbound segment of the profile at higher

–29–
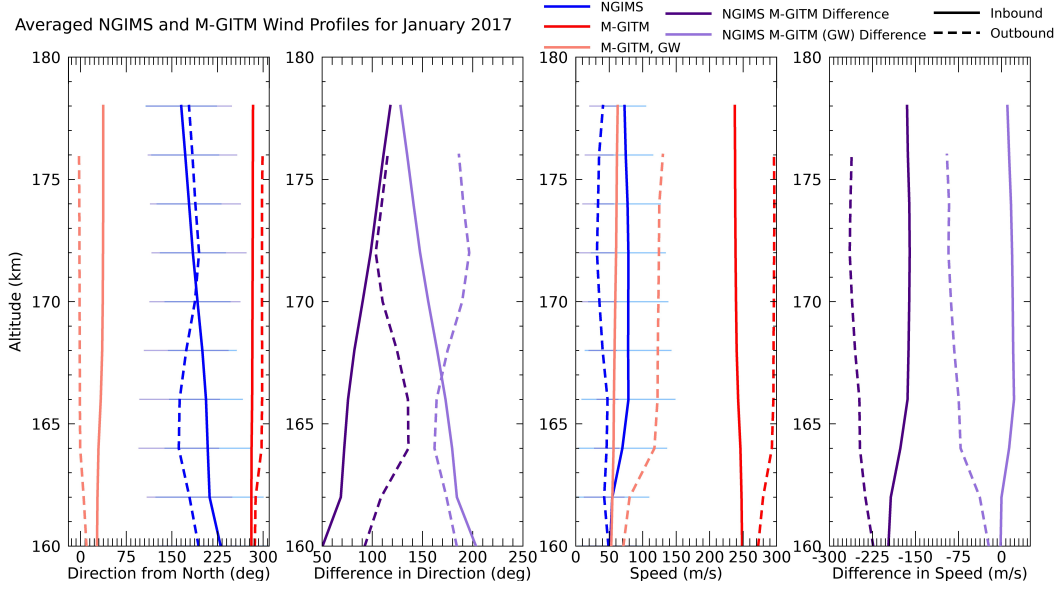
Figure 9. Averaged NGIMS and M-GITM wind profiles for the January 2017 campaign. The first plot shows wind direction (with 0° indicating winds blowing to the north), the second shows difference in direction between the NGIMS observations and model flythroughs, the third shows the wind speed, and the fourth shows the difference in speed between the NGIMS observations and model flythroughs. Blue profiles are NGIMS averages, with horizontal bars showing one standard deviation of orbit-to-orbit variability. Red colors show averaged M-GITM flythroughs, with darker red indicating the M-GITM simulation without the GW parameterization and lighter red indicating the simulation which utilized the GW parameterization. Solid lines show the inbound segment of the trajectory, while dashed lines show the outbound segment.
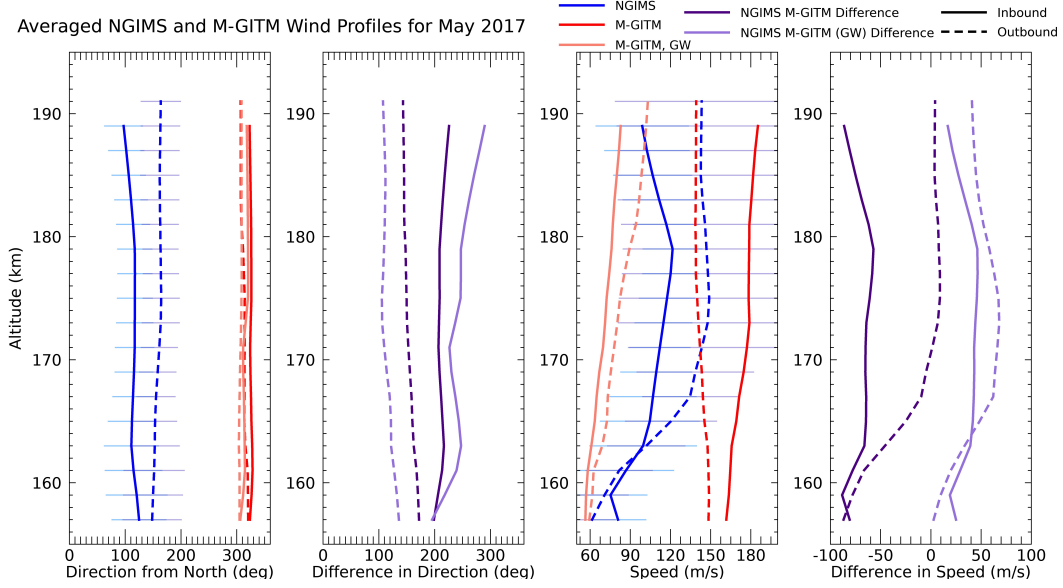
Figure 10. Averaged NGIMS and M-GITM wind profiles for the May 2017 campaign. These plots are set up in the same manner as was described in Figure 9.

altitudes is a reasonable match to averaged speeds observed by the outbound segment of averaged NGIMS data, though the inbound segment is 50-100 m/s faster than observed. Once the GW scheme is added, average simulated speeds decrease by nearly 100 m/s along the profile. This results in a closer match to the observed speeds at the lowest altitudes, but little to no improvement elsewhere. The averaged direction of the simulated velocities shifts negligibly, by less than ten degrees along the profile with the addition of the GW scheme. Notably, the original match between the data and model for the average direction was also poor, being nearly 180° degrees opposed to the direction the model suggests at this local time and latitude sector. The addition of the GW scheme does not discernibly modify this behavior. This might indicate that there are still aspects of the dynamics and circulation in the thermosphere which may be poorly understood and missing from models like M-GITM. Further modeling studies are needed to determine what may be driving this unexpected flow direction.

6 Summary and Conclusions

Gravity waves (GWs) are a key mechanism that facilitates coupling between the lower and upper atmosphere. In order to study the influence of small-scale gravity waves in the Martian thermosphere, a nonlinear whole atmosphere GW parameterization scheme

(Yiğit et al., 2008) has been incorporated into the Mars Global Ionosphere-Thermosphere Model (M-GITM) (Bougher, Pawlowski, et al., 2015) for the first time. Both the GW parameterization scheme and M-GITM are specifically designed to be able to account for physics appropriate for the thermosphere, a region of the atmosphere many other Mars GCMs only partially cover or do not include at all.

Once the parameterized GW momentum deposition and thermal effects are added to the model, zonally and temporally averaged GW drag magnitudes of several hundreds of meters per second per sol are calculated in the thermosphere, particularly within the altitude region spanning 90-170 km. Within this altitude range, GW drag is typically found in two distinct maxima, one in a narrower band of altitudes centered around 90-100 km, and a broader maximum from ∼150-170 km.

M-GITM simulations which included the GW scheme were done for both the southern hemisphere summer solstice ($L_s = 270°$) and southern hemisphere vernal equinox ($L_s = 180°$) seasons. Somewhat larger mean GW drag magnitudes were found in the solstice season as well as a different latitudinal distribution of GW drag due to the changes in background winds with season.

In these M-GITM simulations, momentum deposited by the parameterized sub-grid GWs primarily acts to slow the winds in the upper atmosphere, and particularly in the region from ∼100-150 km, where this decrease in simulated speed effectively acts to close off the jets in the middle atmosphere, which has also seen in other studies (e.g. Medvedev, Yiğit, Hartogh, & Becker, 2011; Yiğit et al., 2018). Throughout the thermosphere (at different latitudes depending on the season), simulated mean zonal winds decrease appreciably (by up to several tens of meters per second) compared to the M-GITM simulation without the GW parameterization scheme. The mean meridional wind response tends to be more complex, and can undergo reversals in direction starting at ∼100 km, particularly during the equinox.

The net thermal effects of the sub-grid GWs in M-GITM lead to a cooler thermosphere at most latitudes than would be otherwise above ∼120 km in simulations of both seasons. Changes in the temperature structure in the model are a result of a combination of the contributions from the GW heating/cooling terms calculated by the GW scheme itself as well as a result of the changes to the background winds in the model, which in turn modifies temperature advection and adiabatic heating. Additionally, the middle at-

–32–

mosphere (∼50-90 km) becomes slightly warmer at the solstice with the addition of the GW scheme to M-GITM.

A series of sensitivity tests was completed wherein certain adjustable parameters within the GW scheme were systematically varied. While results from this testing confirms that the GW scheme is robust within the model, some notable variations can occur in mean upper atmospheric winds and temperature with large changes in the horizontal wavelength and the maximum momentum flux at the source level. When horizontal wavelength is decreased by 100 km, there is an increase in the mean magnitude of momentum deposited at higher altitudes, near ∼140-170 km. As the maximum momentum flux at the source level increases, sub-grid GWs tend to deposit momentum at slightly lower altitudes (a change of ∼10 km when the maximum source flux is doubled).

Two types of comparisons were also shown between M-GITM simulations and thermospheric observations from MAVEN/NGIMS. Comparing a temperature profile from Deep Dip 2, one of NGIMS special observational campaigns, to M-GITM flythroughs, it is found that the addition of the GW parameterization cools down M-GITM's original profile by 10-15 K, bringing it closer to the observed temperatures, particularly above ∼180 km. At these higher altitudes, approaching the exobase, the M-GITM temperature profile now matches the temperature profile derived from NGIMS densities. Comparing examples of NGIMS wind campaigns to the new M-GITM simulation produces mixed results. Again, the net effect of slowing down wind velocities is observed, which in one case improves the data-model comparison, and in the other does not. Thus, while improvements are found in some aspects of data-model comparisons, there are others where still-large differences suggest other physical processes not included in M-GITM may play an important role in driving the observed behavior of the thermospheric winds in certain situations.

Data-model comparisons such as these illustrate that while adding a parameterized GW scheme to M-GITM has made model output more realistic under some conditions, work still needs to be done to better understand the influence of small-scale GW effects at specific local times and latitudes in the thermosphere. The full seven years worth of NGIMS density observations could be employed in a future study to try to better optimize the GW scheme within the model under different conditions. In general, it is challenging to validate modeled gravity wave activity with respect to observations, since there

are a number of different gravity wave retrieval techniques and they can yield different results depending on how the background fields are determined (Sakib & Yiğit, 2022). One of the challenges that remains in using a GW parameterization scheme is that the source GW spectrum is still not well known at Mars, but is likely more complex than the Gaussian used here and may be time-varying. Recent analyses of Mars Climate Sounder observations have been done to better understand and characterize the GWs observed in the lower atmosphere, including orographic and non-orographic contributions (e.g. Heavens et al., 2020, 2022). Analyses such as those, especially in combination with results from high-resolution GCM simulations (e.g. Kuroda et al., 2016) might be able to be applied in the future to better refine the source flux formulation used in GW parameterization schemes. The scheme used in this analysis is specifically for non-orographic waves; however zero phase-speed waves can be included provided that their momentum fluxes are known. Nevertheless, orographic gravity waves are unlikely to affect the conclusions of the presented simulations, since they are much more susceptible to dissipation and saturate at lower altitudes in the atmosphere. Finally, while GW effects are seen to vary in the thermosphere in our results according to season, smaller-scale temporal variability in GW behavior and properties from the source level through the upper atmosphere could occur as a result of large-scale dust storm impacts (e.g. Yiğit, Medvedev, et al., 2021; Kuroda et al., 2020).

Despite the challenges present in including the effects of subgrid GWs into a GCM such as M-GITM, this study demonstrates that these small-scale waves have an appreciable impact on the mean upper atmospheric state, as seen by significant GW momentum deposition at thermospheric altitudes, along with corresponding changes to the neutral velocities and temperature structure in the thermosphere. Since this coupling of the lower and upper atmosphere is important to address at Mars, and small-scale GW effects contribute significantly to this coupling, the inclusion of subgrid GW effects in GCMs should become a standard practice in future modeling applications.

7 Data Availability Statement

The MAVEN/NGIMS densities and neutral wind datasets used in this study are available on the Planetary Data System (Benna et al., 2015). The wind measurements are an NGIMS Level 3, Version 3, Release 1 data product and the neutral densities are an NGIMS Level 2, Version 8, Revision 1 data product. In addition, solar fluxes used

in M-GITM simulations are from the MAVEN/EUVM FISM-M empirical model and are a Level 3, Version 14, Revision 3 data product on the Planetary Data System (Eparvier , 2022). M-GITM output from simulations used in this study can be found at the University of Michigan Deep Blue repository (Roeten et al., 2022).

Acknowledgments

References

Ando, H., Imamura, T., Tsuda, T., Tellmann, S., Pätzold, M., & Häusler, B. (2015). Vertical wavenumber spectra of gravity waves in the venus atmosphere obtained from Venus Express radio occultation data: Evidence for saturation. *J. Atmos. Sci.*, *72*(6), 2318-2329. doi: 10.1175/JAS-D-14-0315.1

Benna, M.& Lyness, E. (2015). MAVEN Neutral Gas and Ion Mass Spectrometer Data [Dataset]. NASA Planetary Data System. doi: 10.17189/1518931

Benna, M., Bougher, S. W., Lee, Y., Roeten, K. J., Yiğit, E., Mahaffy, P. R., & Jakosky, B. M. (2019). Global circulation of Mars' upper atmosphere. *Science*, *366*(6471), 1363-1366. doi: 10.1126/science.aax1553

Bougher, S. W., Bell, J. M., Murphy, J. R., Lopez-Valverde, M. A., & Withers, P. G. (2006). Polar warming in the Mars thermosphere: Seasonal variations owing to changing insolation and dust distributions. *Geophys. Res. Lett.*, *330*, L02203. doi: 10.1029/2005GL024059

Bougher, S. W., Brain, D. A., Fox, J. L., Gonzalez-Galindo, F., Simon-Wedlund, C., & Withers, P. G. (2017). Upper neutral atmosphere and ionosphere. In R. M. Haberle, R. T. Clancy, F. Forget, M. D. Smith, & R. W. Zurek (Eds.), *The Atmosphere and Climate of Mars* (p. 433–463). Cambridge University Press. doi: 10.1017/9781139060172.014

Bougher, S. W., Engel, S., Roble, R. G., & Foster, B. (1999). Comparative terrestrial planet thermospheres 2. Solar cycle variation of global structure and winds at equinox. *J. Geophys. Res.*, *1041*, 16591-16611. doi:

10.1029/1998JE001019

Bougher, S. W., Engel, S., Roble, R. G., & Foster, B. (2000). Comparative terrestrial planet thermospheres 3. Solar cycle variation of global structure and winds at solstices. *J. Geophys. Res.*, *105*, 17669-17692. doi: 10.1029/1999JE001232

Bougher, S. W., Fesen, C. G., Ridley, E. C., & Zurek, R. W. (1993). Mars mesosphere and thermosphere coupling: Semidiurnal tides. *J. Geophys. Res.*, *95(E2)*, 3281–3295. doi: 10.1029/92JE02727

Bougher, S. W., Jakosky, B. M., Halekas, J., Grebowsky, J., Luhmann, J. G., Mahaffy, P., et al. (2015). Early MAVEN dip deep campaign reveals thermosphere and ionosphere variability. *Science*, *350*, 1-7. doi: 10.1126/science.aad0459

Bougher, S. W., Pawlowski, D., Bell, J. M., Nelli, S., McDunn, T., Murphy, J. R., et al. (2015). Mars Global Ionosphere-Thermosphere Model: Solar cycle, seasonal, and diurnal variations of the Mars upper atmosphere. *J. Geophys. Res.*, *120*, 311-342. doi: 10.1002/2014JE004715

Bougher, S. W., Roble, R. G., Ridley, E. C., & Dickinson, R. E. (1990). The Mars thermosphere 2. General circulation with coupled dynamics and composition. *J. Geophys. Res.*, *95(B9)*, 14811–14827. doi: 10.1029/JB095iB09p14811

Bougher, S. W., Roeten, K. J., Olsen, K., Mahaffy, P. R., Benna, M., Elrod, M., et al. (2017). The structure and variability of Mars dayside thermosphere from MAVEN NGIMS and IUVS measurements: Seasonal and solar activity trends in scale heights and temperatures. *Journal of Geophysical Research: Space Physics*, *122*(1), 1296-1313. doi: 10.1002/2016JA023454

Conrath, B. J. (1975). Thermal structure of the Martian atmosphere during the dissipation of the dust storm of 1971. *Icarus*, *24*(1), 36–46. doi: 10.1016/0019-1035(75)90156-6

Creasey, J. E., Forbes, J. M., & Keating, G. M. (2006). Density variability at scales typical of gravity waves observed in Mars' thermosphere by the MGS accelerometer. *Geophysical Research Letters*, *33*(22), L22814. doi: 10.1029/2006GL027583

Elrod, M. K., Bougher, S. W., Roeten, K., Sharrar, R., & Murphy, J. (2020). Structural and compositional changes in the upper atmosphere related to the PEDE-2018 dust event on Mars as observed by MAVEN NGIMS. *Geophysical*

Research Letters, *47*(4), e2019GL084378. doi: 10.1029/2019GL084378

England, S. L., Liu, G., Yiğit, E., Mahaffy, P. R., Elrod, M., Benna, M., et al. (2017). MAVEN NGIMS observations of atmospheric gravity waves in the Martian thermosphere. *Journal of Geophysical Research: Space Physics*, *122*(2), 2310-2335. doi: 10.1002/2016JA023475

Eparvier, F. G. (2022). MAVEN EUV Modelled Data Bundle [Dataset]. NASA Planetary Data System. doi: 10.17189/1517691

Ergun, R. E., Morooka, M. W., Andersson, L. A., Fowler, C. M., Delory, G. T., Andrews, D. J., et al. (2015). Dayside electron temperature and density profiles at Mars: First results from the MAVEN Langmuir probe and waves instrument. *Geophysical Research Letters*, *42*(21), 8846-8853. doi: 10.1002/2015GL065280

Fang, X., Pawlowski, D., Ma, Y., Bougher, S., Thiemann, E., Eparvier, F., et al. (2019). Mars upper atmospheric responses to the 10 September 2017 solar flare: A global, time-dependent simulation. *Geophysical Research Letters*, *46*(16), 9334-9343. doi: 10.1029/2019GL084515

Forbes, J. M., Bruinsma, S. L., Doornbos, E., & Zhang, X. (2016). Gravity wave-induced variability of the middle thermosphere. *J. Geophys. Res. Space Physics*, *121*(7), 6914–6923. doi: 10.1002/2016JA022923

Fritts, D. C., Wang, L., & Tolson, R. H. (2006). Mean and gravity wave structures and variability in the Mars upper atmosphere inferred from Mars Global Surveyor and Mars Odyssey aerobraking densities. *Journal of Geophysical Research: Space Physics (1978–2012)*, *111*, A12304. doi: 10.1029/2006JA011897

González-Galindo, F., Chaufray, J.-Y., López-Valverde, M. A., Gilli, G., Forget, F., Leblanc, F., et al. (2013). 3D Martian Ionosphere model: I. The photochemical ionosphere below 180 km. *Journal of Geophysical Research*, *118*, 2105-2123. doi: 10.1002/jgre.20150

González-Galindo, F., López-Valverde, M. A., Forget, F., García-Comas, M., Millour, E., & Montabone, L. (2015). Variability of the Martian thermosphere during eight Martian years as simulated by a ground-to-exosphere global circulation model. *Journal of Geophysical Research: Planets*, *120*(11), 2020-2035. doi: 10.1002/2015JE004925

Gu, H., Cui, J., Niu, D.-D., Cao, Y.-T., Wu, X.-S., Li, J., et al. (2020). Neutral

–37–

heating efficiency in the dayside Martian upper atmosphere. *The Astronomical Journal*, *159*(2), 39. doi: 10.3847/1538-3881/ab5fcc

Haberle, R. M., Joshi, M. M., Murphy, J. R., Barnes, J. R., Schofield, J. T., Wilson, G., et al. (1999). General circulation model simulations of the Mars Pathfinder atmospheric structure investigation/meteorology data. *Journal of Geophysical Research*, *104*, 8957-8974. doi: 10.1029/1998JE900040

Heavens, N. G., Kass, D. M., Kleinböhl, A., & Schofield, J. T. (2020). A multiannual record of gravity wave activity in Mars's lower atmosphere from on-planet observations by the Mars Climate Sounder. *Icarus*, *341*, 113630. doi: 10.1016/j.icarus.2020.113630

Heavens, N. G., Pankine, A., Battalio, J. M., Wright, C., Kass, D. M., Kleinböhl, A., et al. (2022). Mars Climate Sounder observations of gravity-wave activity throughout Mars's lower atmosphere. *The Planetary Science Journal*, *3*(3), 57. doi: 10.3847/psj/ac51ce

Hinson, D., Pätzold, M., Tellmann, S., Häusler, B., & Tyler, G. (2008). The depth of the convective boundary layer on Mars. *Icarus*, *198*(1), 57-66. doi: 10.1016/j.icarus.2008.07.003

Jain, S. K., Bougher, S. W., Deighan, J., Schneider, N. M., González Galindo, F., Stewart, A. I. F., et al. (2020). Martian thermospheric warming associated with the planet encircling dust event of 2018. *Geophysical Research Letters*, *47*(3), e2019GL085302. doi: 10.1029/2019GL085302

Jakosky, B. M., Lin, R. P., Grebowksy, J. M., Luhmann, J. G., Mitchell, D. F., Beutelschies, G., et al. (2015). The Mars Atmosphere and Volatile Evolution (MAVEN) Mission. *Space Sci. Reviews*, *195*, 3-48. doi: 10.1007/s11214-015-0139-x

Jesch, D., Medvedev, A. S., Castellini, F., Yiğit, E., & Hartogh, P. (2019). Density fluctuations in the lower thermosphere of Mars retrieved from the ExoMars Trace Gas Orbiter (TGO) aerobraking. *Atmosphere*, *10*(10), 620. doi: 10.3390/atmos10100620

Kuroda, T., Medvedev, A. S., & Yiğit, E. (2020). Gravity wave activity in the atmosphere of Mars during the 2018 global dust storm: Simulations with a high-resolution model. *Journal of Geophysical Research: Planets*, *125*(11), e2020JE006556. doi: 10.1029/2020JE006556

Kuroda, T., Medvedev, A. S., Yiğit, E., & Hartogh, P. (2016). Global distribution of gravity wave sources and fields in the Martian atmosphere during equinox and solstice inferred from a high-resolution general circulation model. *Journal of the Atmospheric Sciences*, *73*(12), 4895 - 4909. doi: 10.1175/JAS-D-16-0142.1

Leelavathi, V., Venkateswara Rao, N., & Rao, S. V. B. (2020). Interannual variability of atmospheric gravity waves in the Martian thermosphere: Effects of the 2018 planet-encircling dust event. *J. Geophys. Res. Planets*, *125*(12), e2020JE006649. doi: 10.1029/2020JE006649

Lilienthal, F., Yiğit, E., Samtleben, N., & Jacobi, C. (2020). Variability of gravity wave effects on the zonal mean circulation and migrating terdiurnal tide as studied with the middle and upper atmosphere model (MUAM2019) using a nonlinear gravity wave scheme. *Front. Astron. Space Sci.*, *2020*(7), 588956. doi: 10.3389/fspas.2020.588956

Mahaffy, P. R., Benna, M., Elrod, M., Yelle, R. V., Bougher, S. W., Stone, S. W., & Jakosky, B. M. (2015). Structure and composition of the neutral upper atmosphere of Mars from the MAVEN NGIMS investigation. *Geophys. Res. Lett.*, *42*, 8951-8957. doi: 10.1002/2015GL065329

Mahaffy, P. R., Benna, M., King, T., Harpold, D. N., Arvey, R., Barciniak, M., et al. (2015). The Neutral Gas and Ion Mass Spectrometer on the Mars Atmosphere and Volatile Evolution Mission. *Space Sci. Reviews*, *195*, 49-73. doi: 10.1007/s11214-014-0091-1

Medvedev, A. S., González-Galindo, F., Yiğit, E., Feofilov, A. G., Forget, F., & Hartogh, P. (2015). Cooling of the Martian thermosphere by CO_2 radiation and gravity waves: An intercomparison study with two general circulation models. *J. Geophys. Res. Planets*, *120*, 913-927. doi: 10.1002/2015JE004802

Medvedev, A. S., & Klaassen, G. P. (2000). Parameterization of gravity wave momentum deposition based on nonlinear wave interactions: Basic formulation and sensitivity tests. *Journal of Atmospheric and Solar-Terrestrial Physics*, *62*, 1015-1033. doi: 10.1016/S1364-6826(00)00067-5

Medvedev, A. S., Nakagawa, H., Mockel, C., Yiğit, E., Kuroda, T., Hartogh, P., et al. (2016). Comparison of the Martian thermospheric density and temperature from IUVS/MAVEN data and general circulation modeling. *Geophys. Res.*

–39–

Lett., *43*(7), 3095–3104. doi: 10.1002/2016GL068388

Medvedev, A. S., & Yiğit, E. (2012). Thermal effects of internal gravity waves in the Martian upper atmosphere. *Geophys. Res. Lett.*, *39*, L05201. doi: 10.1029/2012GL050852

Medvedev, A. S., & Yiğit, E. (2019). Gravity waves in planetary atmospheres: Their effects and parameterization in global circulation models. *Atmosphere*, *10*(9), 531. doi: 10.3390/atmos10090531

Medvedev, A. S., Yiğit, E., & Hartogh, P. (2011). Estimates of gravity wave drag on Mars: indication of a possible lower thermosphere wind reversal. *Icarus*, *211*, 909–912. doi: 10.1016/j.icarus.2010.10.013

Medvedev, A. S., Yiğit, E., & Hartogh, P. (2017). Ion friction and quantification of the geomagnetic influence on gravity wave propagation and dissipation in the thermosphere-ionosphere. *J. Geophys. Res. Space Physics*, *122*(12), 12464-12475. doi: 10.1002/2017JA024785

Medvedev, A. S., Yiğit, E., Hartogh, P., & Becker, E. (2011). Influence of gravity waves on the Martian atmosphere: General circulation modeling. *J. Geophys. Res.*, *116*, E10004. doi: 10.1029/2011JE003848

Medvedev, A. S., Yiğit, E., Kuroda, T., & Hartogh, P. (2013). General circulation modeling of the Martian upper atmosphere during global dust storms. *J. Geophys. Res. Planets*, *118*, 1–13. doi: 10.1002/2013JE004429

Miyoshi, Y., & Yiğit, E. (2019). Impact of gravity wave drag on the thermospheric circulation: Implementation of a nonlinear gravity wave parameterization in a whole atmosphere model. *Annales Geophysicae*, *37*, 955–969. doi: 10.5194/angeo-37-955-2019

Parish, H. F., Schubert, G., Hickey, M., & Walterscheid, R. L. (2009). Propagation of tropospheric gravity waves into the upper atmosphere of Mars. *Icarus*, *203*, 28–37. doi: 10.1016/j.icarus.2009.04.031

Ridley, A., Deng, Y., & Tòth, G. (2006). The Global Ionosphere-Thermosphere Model. *J. Atmos. Sol-Terr. Phys.*, *68*, 839. doi: 10.1016/j.jastp.2006.01.008

Roeten, K. J., Bougher, S. W., Benna, M., Mahaffy, P. R., Lee, Y., Pawlowski, D., et al. (2019). MAVEN/NGIMS thermospheric neutral wind observations: Interpretation using the M-GITM general circulation model. *Journal of Geophysical Research: Planets*, *124*(12), 3283-3303. doi: 10.1029/2019JE005957

–40–

Roeten, K. J. & Bougher, S. W. (2022). M-GITM datasets used for a modeling study of the mean impacts of subgrid-scale gravity waves on thermospheric velocities and temperatures at Mars [Dataset]. University of Michigan - Deep Blue Data. doi: 10.7302/7hab-2340

Rohrbaugh, R., Nisbet, J., Bleuler, E., & Herman, J. (1979). The effect of energetically produced O_2^+ on the ion temperatures of the Martian thermosphere. *Journal of Geophysical Research: Space Physics*, *84*(A7), 3327-3338. doi: 10.1029/JA084iA07p03327

Sakib, M. N., & Yiğit, E. (2022). A brief overview of gravity wave retrieval techniques from observations. *Front. Astron. Space Sci.*, *9*, 824875. doi: 10.3389/fspas.2022.824875

Shaposhnikov, D. S., Medvedev, A. S., Rodin, A. V., & Hartogh, P. (2019). Seasonal water "pump" in the atmosphere of Mars: Vertical transport to the thermosphere. *Geophys. Res. Lett.*, *46*(8), 4161–4169. doi: 10.1029/2019GL082839

Shaposhnikov, D. S., Medvedev, A. S., Rodin, A. V., Yiğit, E., & Hartogh, P. (2022). Martian dust storms and gravity waves: Disentangling water transport to the upper atmosphere. *J. Geophys. Res. Planets*, *127*(1), e2021JE007102. doi: 10.1029/2021JE007102

Siddle, A., Mueller-Wodarg, I., Stone, S., & Yelle, R. (2019). Global characteristics of gravity waves in the upper atmosphere of Mars as measured by MAVEN/NGIMS. *Icarus*, *333*, 12-21. doi: 10.1016/j.icarus.2019.05.021

Snowden, D., Yelle, R.-V., Cui, J., Wahlund, J.-E., Edberg, N. J. T., & Agren, K. (2013). The thermal structure of Titan's upper atmosphere: 1. Temperature profiles from Cassini INMS observations. *Icarus*, *226*, 552-582. doi: 10.1016/j.icarus.2013.06.006

Starichenko, E. D., Belyaev, D. A., Medvedev, A. S., Fedorova, A. A., Korablev, O. I., Trokhimovskiy, A., et al. (2021). Gravity wave activity in the Martian atmosphere at altitudes 20–160 km from ACS/TGO occultation measurements. *Journal of Geophysical Research: Planets*, *126*(8), e2021JE006899. doi: 10.1029/2021JE006899

Stone, S. W., Yelle, R. V., Benna, M., Elrod, M. K., & Mahaffy, P. R. (2018). Thermal structure of the Martian upper atmosphere from MAVEN NGIMS. *Journal of Geophysical Research: Planets*, *123*(11), 2842-2867. doi:

10.1029/2018JE005559

Terada, N., Leblanc, F., Nakagawa, H., Medvedev, A. S., Yiğit, E., Kuroda, T., et al. (2017). Global distribution and parameter dependences of gravity wave activity in the Martian upper thermosphere derived from MAVEN/NGIMS observations. *Journal of Geophysical Research: Space Physics*, *122*(2), 2374-2397. doi: 10.1002/2016JA023476

Thiemann, E. M. B., Chamberlin, P. C., Eparvier, F. G., Templeman, B., Woods, T. N., Bougher, S. W., & Jakosky, B. M. (2017). The MAVEN EUVM model of solar spectral irradiance variability at Mars: Algorithms and results. *Journal of Geophysical Research: Space Physics*, *122*(3), 2748-2767. doi: 10.1002/2016JA023512

Tolson, R., Keating, G., Zurek, R., Bougher, S., Justus, C., & Fritts, D. (2007). Application of acclerometer data to atmospheric modeling during Mars aerobraking operations. *Journal of Spacecraft and Rockets*, *44*(6), 1172–1179. doi: 10.2514/1.28472

Vals, M., Spiga, A., Forget, F., Millour, E., Montabone, L., & Lott, F. (2019). Study of gravity waves distribution and propagation in the thermosphere of Mars based on MGS, ODY, MRO, and MAVEN density measurements. *Planetary and Space Science*, *178*, 104708. doi: 10.1016/j.pss.2019.104708

Watanabe, S., & Miyahara, S. (2009). Quantification of the gravity wave forcing of the migrating diurnal tide in a gravity wave–resolving general circulation model. *J. Geophys. Res.*, *114*, D07110. doi: 10.1029/2008JD011218

Yiğit, E., Medvedev, A. S., & Hartogh, P. (2021). Variations of the Martian thermospheric gravity-wave activity during the recent solar minimum as observed by MAVEN. *APJ*, *920*(2), 69. doi: 10.3847/1538-4357/ac15fc

Yiğit, E., Alexander, A. S., & Ern, M. (2021). Effects of latitude-dependent gravity wave source variations on the middle and upper atmosphere. *Front. Astron. Space Sci.*, *7*, 614018. doi: 10.3389/fspas.2020.614018

Yiğit, E., Aylward, A. D., & Medvedev, A. S. (2008). Parameterization of the effects of vertically propagating gravity waves for thermosphere general circulation models: Sensitivity study. *J. Geophys. Res.*, *113*, D19106. doi: 10.1029/2008JD010135

Yiğit, E., & Medvedev, A. S. (2009). Heating and cooling of the thermosphere

by internal gravity waves. *Geophys. Res. Lett.*, *36*, L14807. doi: 10.1029/2009GL038507

Yiğit, E., & Medvedev, A. S. (2015). Internal wave coupling processes in Earth's atmosphere. *Adv. Space Res.*, *55*(5), 983–1003. doi: 10.1016/j.asr.2014.11.020

Yiğit, E., & Medvedev, A. S. (2019). Obscure waves in planetary atmospheres. *Physics Today*, *6*, 40-46. doi: 10.1063/PT.3.4226

Yiğit, E., Medvedev, A. S., Aylward, A. D., Hartogh, P., & Harris, M. J. (2009). Modeling the effects of gravity wave momentum deposition on the general circulation above the turbopause. *J. Geophys. Res.*, *114*, D07101. doi: 10.1029/2008JD011132

Yiğit, E., Medvedev, A. S., Benna, M., & Jakosky, B. M. (2021). Dust storm-enhanced gravity wave activity in the Martian thermosphere observed by MAVEN and implication for atmospheric escape. *Geophysical Research Letters*, *48*(5), e2020GL092095. doi: 10.1029/2020GL092095

Yiğit, E., Medvedev, A. S., & Hartogh, P. (2018). Influence of gravity waves on the climatology of high-altitude Martian carbon dioxide ice clouds. *Annales Geophysicae*, *36*(6), 1631–1646. doi: 10.5194/angeo-36-1631-2018

Yiğit, E., England, S. L., Liu, G., Medvedev, A. S., Mahaffy, P. R., Kuroda, T., & Jakosky, B. M. (2015). High-altitude gravity waves in the Martian thermosphere observed by MAVEN/NGIMS and modeled by a gravity wave scheme. *Geophysical Research Letters*, *42*(21), 8993-9000. doi: 10.1002/2015GL065307

Zurek, R. W., Tolson, R. A., Bougher, S. W., Lugo, R. A., Baird, D. T., Bell, J. M., & Jakosky, B. M. (2017). Mars thermosphere as seen in MAVEN accelerometer data. *Journal of Geophysical Research: Space Physics*, *122*(3), 3798-3814. doi: 10.1002/2016JA023641